Sustainable Energy, Grids and Networks 38 (2024) 101337

Contents lists available at ScienceDirect

Sustainable Energy, Grids and Networks

journal homepage: www.elsevier.com/locate/segan

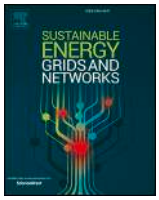

Time-dependent photovoltaic performance assessment on a global scale using artificial neural networks

Nicoletta Matera *, Michela Longo, Sonia Leva

Department of Energy, Politecnico di Milano, Milan IT-20156, Italy

ARTICLE INFO

Keywords:
Machine learning
Artificial neural network
Photovoltaic
5-parameter model
Electrical energy

ABSTRACT

The integration of Renewable Energy Sources (RESs), particularly solar PhotoVoltaics (PVs) has become an imperative aspect of sustainable energy systems. In this pursuit, accurate and efficient simulation tools play a pivotal role in optimizing the performance of PV systems. Traditional simulation approaches, while effective, are often characterized by computational complexities and time-intensive processes. This paper introduces a groundbreaking paradigm in solar energy modeling by harnessing the power of Artificial Neural Networks (ANNs) to revolutionize the accuracy and reliability of PV system simulations. In this work, an hourly, daily, monthly and yearly comparison of the electrical energy obtained with the 5-parameter model and those obtained with the ANNs was developed. For this purpose, a very wide ensemble of localities around the world and types of PV systems were considered in the training and validation phase. ANNs exhibited a maximum mean absolute relative error of 3.5% during training and consistently maintained hourly relative errors below 5% across diverse localities during validation. Hourly power forecasting remains acceptable also in localities with extreme weather conditions. Monthly errors peak at high negative and positive latitudes in summer months when daylight duration exceeds nighttime. However, in the least accurate locality, yearly energy forecasting yielded a maximum error of 8%. Empirical equations based on the trained ANNs are proposed and a relative input-output importance criterion was applied to detect the impact of air temperature and solar radiation on the performance of each PV module. The proposed ANNs demonstrate significant utility in decision-making and real-time processes, providing a valuable framework for managing energy flows within a network and predicting energy production during specific time intervals. This alternative approach surpasses conventional dynamic simulation methodologies found in existing literature in terms of computational cost with comparable accuracy.

1. Introduction

The rise of distributed PhotoVoltaic (PV) generators in distribution grids decreases reliance on centralized power plants. The variability in solar irradiance presents challenges like voltage fluctuations, reverse power flows, and power quality issues that can be addressed by considering various methods aiming to control voltage and minimize violations [1]. The effective utilization of solar energy is hindered by the need for expensive storage infrastructure to handle power fluctuations, and, in the absence of viable storage, the potential necessity for energy curtailment during peak production hours in the presence of high renewable energy diffusion [2]. These aspects and challenges have underscored the need for precise and expeditious tools to model and optimize the performance of PV systems [3,4]. While conventional numerical methods and analytical models have proven their utility in simulating solar energy generation, the increasing complexity of PV technologies and the dynamic nature of environmental conditions necessitate novel approaches to enhance simulation accuracy and reduce computational overhead. Artificial Neural Networks (ANNs), inspired by the structure and function of the human brain, have emerged as a promising avenue for addressing the limitations of traditional simulation methods. They found a large application in the energy system field in the last decades [5–7]. ANNs possess the ability to learn intricate patterns and relationships within vast datasets, allowing them to capture the nonlinear and time-varying behaviors inherent in solar energy systems [8–11]. However, the large dependency of PV power on weather conditions brings a major challenge of uncertainty to system operation and efficiency [12]. To address this dilemma, an accurate and reliable forecast of PV power production is essential to stabilize and secure the PV electricity supply.

Overall, ANN techniques have emerged as effective tools in modern

* Corresponding author.
E-mail address: nicoletta.matera@polimi.it (N. Matera).

https://doi.org/10.1016/j.segan.2024.101337
Received 24 January 2024; Received in revised form 28 February 2024; Accepted 4 March 2024
Available online 6 March 2024

Nomenclature

a/c	Weighted circumsolar solid angle [-]
b_i	Bias vector of the i-th layer in an ANN architecture
A	PV module area [m^2]
E_g	yearly PV energy generated [Wh]
F_1'	Reduced brightness coefficient (circumsolar) [-]
F_2'	Reduced brightness coefficient (horizon brightening) [-]
F_{ij}	Perez coefficients [-]
g_h	Dimensionless horizontal total solar radiation [-]
G	Total radiation on the horizontal surface [W/m^2]
G_{avg}	Yearly average total radiation on the horizontal surface [W/m^2]
G_b	Beam radiation on the horizontal surface [W/m^2]
G_{bT}	Beam radiation on the tilted surface [W/m^2]
G_d	Diffuse radiation on the horizontal surface [W/m^2]
G_{dn}	Direct normal beam radiation [W/m^2]
G_{dT}	Diffuse radiation on the tilted surface [W/m^2]
G_{ex}	Extraterrestrial radiation [W/m^2]
$G_{ex,n}$	Extraterrestrial radiation at normal incidence [W/m^2]
G_{gT}	Ground reflected radiation on the tilted surface [W/m^2]
G_h	Hourly total horizontal solar radiation [W/m^2]
$G_{h,ref}$	Reference radiation of 1000 W/m^2 [W/m^2]
G_{sd}	Yearly standard deviation of the total radiation on a horizontal surface [W/m^2]
G_T	Total radiation on the tilted surface [W/m^2]
$G_{T,eff}$	Effective total radiation incident on the PV array [W/m^2]
$G_{T,NOCT}$	Incident radiation at NOCT conditions [W/m^2]
$G_{T,ref}$	Incident radiation at reference conditions [W/m^2]
I	Current [A]
I_o	Diode reverse saturation current [A]
$I_{o,ref}$	Diode reverse saturation current at reference conditions [A]
I_{sc}	Short-circuit current [A]
$I_{sc,ref}$	Short-circuit current at reference conditions [A]
I_L	Module photocurrent [A]
$I_{L,ref}$	Module photocurrent at reference conditions [A]
I_{mp}	Current at maximum power point along IV curve [A]
$I_{mp,ref}$	Current at maximum power point along IV curve, reference conditions [A]
IAM	Dimensionless incidence angle modifier [-]
IAM_{beam}	Dimensionless incidence angle modifier for the beam radiation [-]
IAM_{gnd}	Dimensionless incidence angle modifier for the ground reflected diffuse radiation [-]
IAM_{diff}	Dimensionless incidence angle modifier for the sky diffuse radiation [-]
k	Boltzmann constant [J/K]
l	number of layers in the ANN
L	Latitude [degrees]
m	air mass [-]
n	number of weights
n_i	Number of neurons in the i-the ANN layer
N	Number of training data
N_{cs}	Number of individual cells in module [-]
N_R	Number of routes between each input and output neuron
NOCT	Nominal operating cell temperature [°C]
p_{el}	Dimensionless electrical PV power produced [-]
$p_{el,n}$	Normalized dimensionless electrical PV power produced [-]
P_{el}	Hourly electrical PV power produced [W]
P_{pv}	PV output power [W]
P_{mp}	PV output power at maximum power point along I-V curve [W]
P_{pv}	Power produced by the photovoltaic generator [W]
$P_{pv,n}$	Nominal power of the photovoltaic generator [W]
q	Electron charge constant [C]
R_b	Ratio of beam radiation on the tilted surface to the beam radiation on the horizontal surface [-]
R_r	Ratio of reflected radiation on the tilted surface to the total radiation on the horizontal surface [-]
R_s	Module series resistance [Ω]
R_{sh}	Module shunt resistance [Ω]
R^2	R-square [-]
s_{ij}	Sum of the r overall weights $W_{r,ij}$
S_{ij}	Percentage sensitivity index
t	Time (s)
t_{ea}	Dimensionless air temperature [-]
T_{ea}	Ambient temperature [K]
$T_{ea,avg}$	Yearly average ambient temperature [K]
$T_{ea,ref}$	Reference temperature of 25° C [K]
$T_{ea,sd}$	Yearly standard deviation of the ambient temperature [K]
T_c	Cell temperature [K]
$T_{c,NOCT}$	Cell temperature at NOCT conditions [K]
$T_{c,ref}$	Cell temperature at reference conditions [K]
U_L	PV thermal loss coefficient [W/m^2 K]
V	Voltage [V]
V_{oc}	Open-circuit voltage [V]
$V_{oc,ref}$	Open-circuit voltage at reference conditions [V]
V_{mp}	Voltage at maximum power point along IV curve [V]
$V_{mp,ref}$	Voltage at maximum power point along IV curve at reference conditions [V]
$W_{r,ij}$	r-th overall weight
w_i	Weight matrix between the (i-1)-th layer and the i-th layer in an ANN architecture
x_0	Input vector with n_0 nodes in an ANN architecture
y	Output vector of the ANN
y_i	i-th value of the output

Greek letters

β	Slope of surface, positive when tilted in the direction of the azimuth specification [degrees]
δ	Solar declination angle [degrees]
Δ	Sky brightness parameter [-]
ε	Sky clearness parameter [-]
φ	Activation function in an ANN architecture
γ	Empirical PV curve-fitting parameter [-]
γ_{su}	Azimuth angle of surface; angle between the projection of the normal to the surface into the horizontal plane and the local meridian. (facing equator = 0, west positive, east negative) [degrees]
γ_{so}	Solar azimuth angle [degrees]
μ_{Isc}	Temperature coefficient of short-circuit current [%/K]
μ_{Voc}	Temperature coefficient of open-circuit voltage [%/K]
η_m	Module conversion efficiency
θ	Angle of incidence of the beam radiation on the surface [degrees]
θ_Z	Solar zenith angle [degrees]
$\theta_{eff,gnd}$	Effective angle of incidence for the ground reflected diffuse radiation [degrees]
$\theta_{eff,diff}$	Effective angle of incidence for the sky diffuse radiation [degrees]
ρ_g	Ground reflectance [-]
ω	Mean hour angle of time step (0 at noon, mornings negative) [degrees]
τα	Module transmittance-absorptance product [-]
$\tau\alpha_{normal}$	Module transmittance-absorptance product at normal incidence [-]

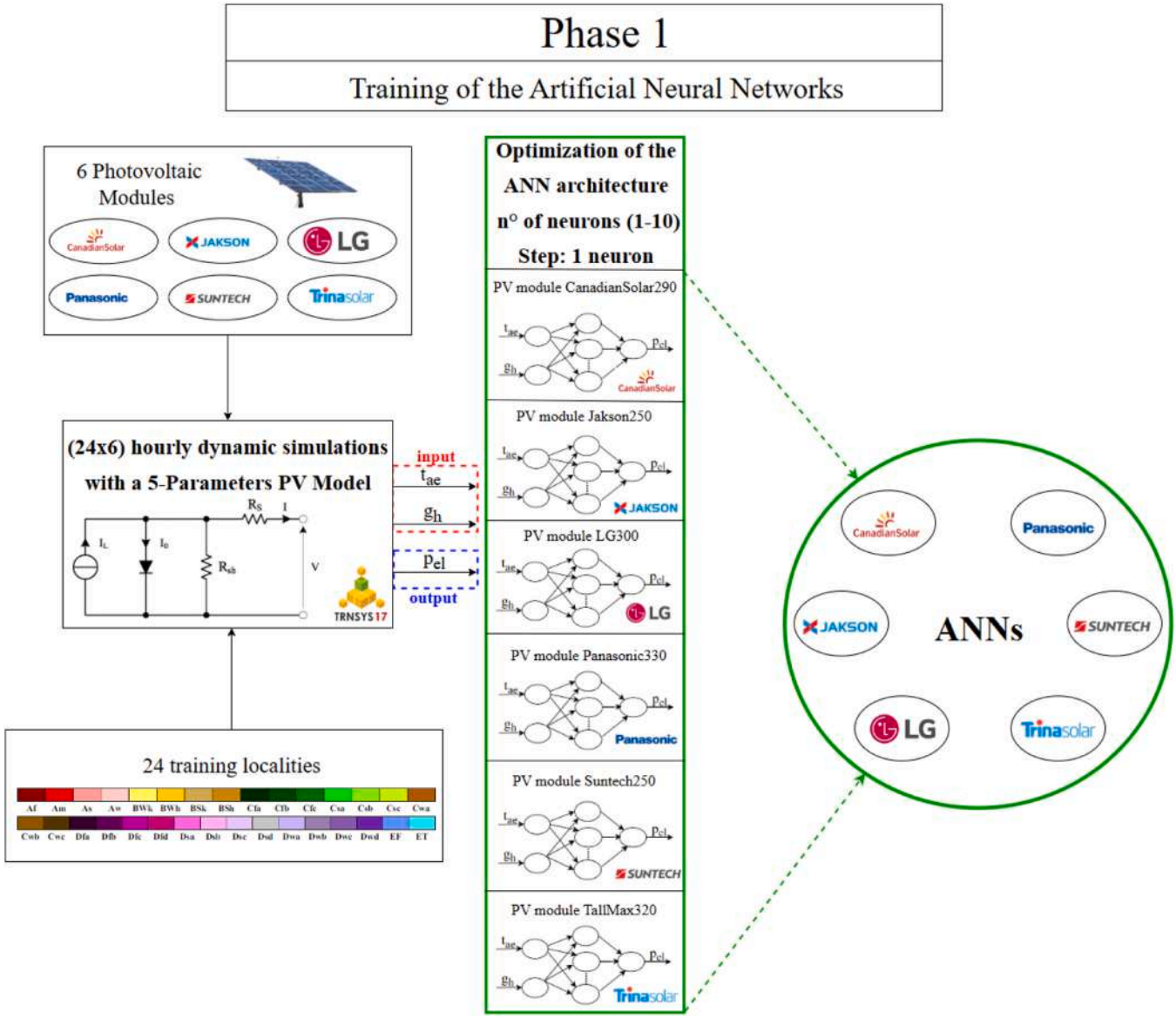

Fig. 1. Framework of Phase 1 for the Training of the artificial neural networks.

power system applications such as sustainable operation considering renewable uncertainties [13], PV fault detection and diagnosis [14], adaptive protection and control [15], and smart generation dispatch [16]. Das et al. presented a comprehensive and systematic review of various models including statistical and Machine-Learning (ML) models of the direct forecasting of PV power generation, highlighting the strengths and weaknesses of each approach [17]. Considering the expected accuracy and less complexity of the ANN approach becomes the most used ML method [18]. Apart from recent literature, Qin et al. [19] established an innovative strategy that integrates ground and satellite observations through deep learning to strengthen the PV output predictions. Abdullah et al. [20] introduced a communication-free monitoring technique for a remote grid-connected PV plant using ANN and impedance relay measurements from the switchgear panel to assess PV power generation and load consumption. Roseline et al. [21] developed a data-driven ANN model for energy estimation of PV and hybrid PV/wind power systems considering several weather factors. Instead, Weerasinghe et al. [22] presented a methodology for guiding building intenerated PV system applications with the application of commercial buildings, in which a support vector machine prediction model is applied. Another research employed ANN models to investigate the influence of coolant mass flow rate and atmospheric variables on key parameters, including electrical power production and thermal energy, in a PV/Thermal (PV/T) system [23]. Tavares et al. compared and analyzed two PV generation forecasting approaches based on a multi-layer feed-forward ANN and a deep NN with a case study on a multi-apartment residential building [24]. Ghenai et al. [25] proposed a predictive ANN model to anticipate the power output from bifacial solar PV systems installed on flat roof buildings with low and high surface albedo in Sharja, United Arab Emirates. Machine learning was also utilized for improved integration of PV power into day-ahead and intra-day Markets through a tool comprising four specialized Deep Learning forecasters aligned with auction rules [26]. Lee et al. [27] investigated two forecasting models by using long short-term memory and gate recurrent networks for hourly PV power output prediction in a peak zone using real data from Gumi City, South Korea. Most recently, Wang et al. [28] proposed an uncertainty modeling technique of weather data sets for robust PV energy generation of a building through a combined dual-stage attention-based recurrent ANN and Bayesian recurrent ANN.

The key objectives in this field are represented by the investigation of the capacity of ANNs to effectively capture the multifaceted

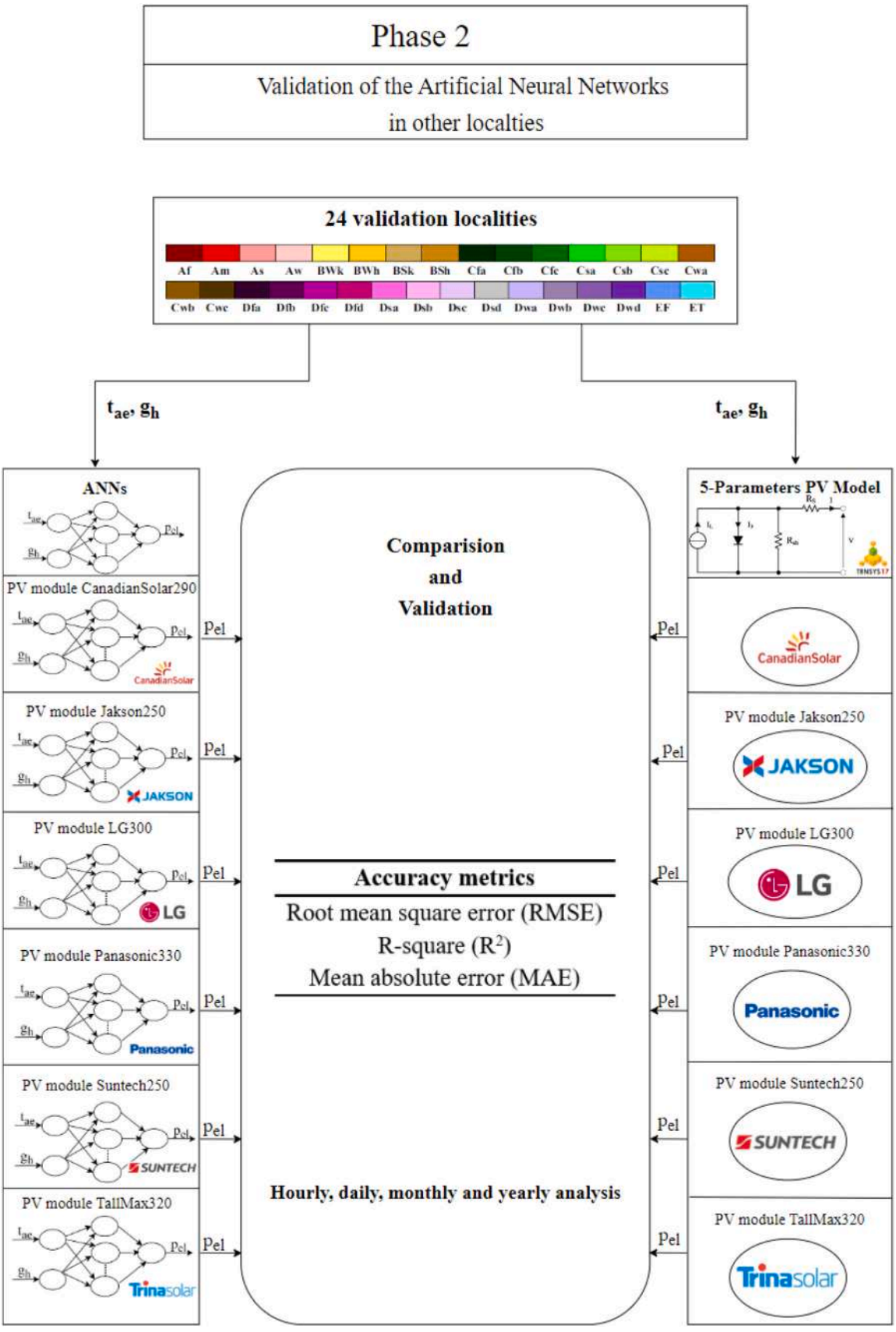

Fig. 2. Framework of Phase 2 for the Validation of the artificial neural networks in other localities.

relationships between various PV system parameters, environmental variables, and energy output and the exploration of the ability of ANNs to adapt and generalize across different PV technologies, ensuring applicability to a broad spectrum of solar energy systems. Another challenging aspect is to assess methodologies for preprocessing and selecting training datasets to enhance the robustness and generalization of the neural network models.

Research trends indicate the importance of exploring strategies to optimize neural network architectures and parameters, aiming to achieve a balance between accuracy and computational speed. It is also crucial to compare the performance of ANN-based models with traditional simulation methods, establishing benchmarks and demonstrating the potential of this innovative approach. In addition, many ANN models for PV performance evaluation are trained and tested on a specific dataset and may not generalize well to different conditions or environments.

Further research is needed to fully understand the potential and limitations of the application of ANNs for PV performance evaluation and to improve their generalization and robustness.

By addressing these objectives and research gaps, this paper aims to present a comprehensive analysis of the transformative impact that ANNs can have on the field of PV simulation. This work explores the application of ANNs as a tool for PV simulation, aiming to provide a tool for hourly, monthly, and yearly prediction of solar energy produced to be used worldwide for different types of PV modules.

The ANNs proposed were trained, optimized, validated and, finally, translated into empirical mathematical equations to evaluate even more easily PV modules performance. The last analysis based on the Garson method aims to evaluate for each PV module the impact of air temperature and solar radiation on the power produced by using the characteristic parameters of the ANNs.

This study is structured as follows: Section 2 provides an account of the research phases and methodologies concerning the training, optimization, and validation of ANNs for forecasting the performance of PV modules; additionally, it details the utilization of a 5-parameter model for generating ANN training and validation datasets across diverse geographical locations and various types of PV modules; Section 3 presents the electrical and thermal characteristics of PV modules, alongside the climatic data for 48 different locations utilized in the training and validation of ANNs; furthermore, it outlines the dimensionless ANN inputs and outputs employed in the analysis; Section 4 delineates the outcomes of the ANN training and optimization processes, including validation results spanning hourly, monthly, and yearly results; finally, Section 5 encapsulates the principal discoveries of the research and outlines prospective directions for future investigations.

2. Methodology

The investigation unfolds in two phases, as depicted in Figs. 1 and 2. In the first phase, six Artificial Neural Networks (ANNs) were established, each dedicated to predicting hourly electrical power for one of six different PV modules, characterized by different electrical and thermal behavior. The sample of PV modules was chosen to consider a wide range of existing PV modules in terms of performance in the standard test conditions. Employing MATLAB's Neural Net Fitting tool, hourly temperature, and horizontal total solar radiation values for 24 locations were input as features, while the corresponding hourly power, obtained with a 5-parameter PV model, served as the output. ANNs underwent training with varied hidden layer neuron counts (1−10), and the optimal neuron count was determined based on some common accuracy metrics.

In the second phase, each ANN underwent validation using hourly temperature and solar radiation data from 24 additional locations, generating corresponding hourly electrical power predictions. A comparative analysis was then conducted between these predictions and those derived from a 5-parameter PV module. The obtained electrical powers, both from the 5-parameter PV module and the best-performing ANN, were employed to assess the ANN's accuracy in terms of hourly, daily, monthly, and yearly energies. This process was replicated for six PV modules with distinct electrical characteristics, establishing six ANNs capable of predicting hourly power for each module across various locations, solely relying on hourly temperature and solar radiation inputs, without recourse to the 5-parameter model.

In the subsequent subsections, the 5-parameter PV model and the ANN model used for this research are extensively presented.

2.1. Modeling and dynamic simulation of PV modules using the 5-parameter model

The dynamic electrical and thermal performance of the solar PV systems considered in this study were simulated using TRNSYS 17 software [29] using a 5-parameter model. TRNSYS is a research simulation program primarily used in the fields of renewable energy engineering and building simulation for passive as well as active solar design. The specific Types available in standard and supplementary libraries in TRNSYS are used for the simulation of the dynamic behavior of each component in the system:

- Type 15 for the generation and importing of the weather data into the TRNSYS environment;
- Type 94 for the simulation of a PV module with a 5-parameter module.

2.1.1. Type 15: Weather data processor and mathematical model for the generation of global solar radiation on the tilted surface

This module interprets various standardized weather data formats, including TMY, TMY2, EnergyPlus Weather, IWEC, and CWEC files. Type 15 computes total, beam, sky diffuse, and ground-reflected solar radiation, along with the angle of incidence for beam solar radiation, and the slope and azimuth for user-defined surfaces. Additionally, it calculates mains water temperature and effective sky temperature for radiation calculations. The output includes indicators for heating and cooling seasons, monthly and annual temperature extremes, and averages. For estimating total tilted surface radiation, the models in this subroutine require knowledge of the division of total horizontal radiation into beam and diffuse components. Correlations are available to estimate beam or diffuse radiation when only total horizontal radiation is measured, with options for calculating total radiation on a tilted surface within Type 15 [30].

2.1.1.1. Position of the sun in the sky. The location of the sun in the sky can be determined by indicating the solar zenith and solar azimuth angles. s. The zenith angle is the measurement between the vertical and the sun's line of sight, calculated as 90 degrees minus the angle between the sun and the horizontal (solar altitude angle). Meanwhile, the solar azimuth angle (θ_z)is determined as the angle between the local meridian and the projection of the sun's line of sight onto the horizontal plane (see Eq. (1)). A solar azimuth of zero points towards the equator, with positive values in the west and negative values in the east. Both zenith and solar angles (γ_{so}) can be derived using the trigonometric relationship, as provided by Duffie and Beckman [30] as shown in Eq. (2).

$$\cos\theta_z = \sin\delta\sin L + \cos L\cos\delta\cos\omega \tag{1}$$

$$\sin\gamma_{so} = \frac{\cos\delta\sin\omega}{\sin\theta_z} \tag{2}$$

2.1.1.2. Tilted surface radiation mode. Models for estimating the total radiation on a tilted surface require knowledge of total and diffuse (or beam) radiation on a horizontal surface as well as the sun's position. In general, the total tilted surface radiation is calculated by estimating and

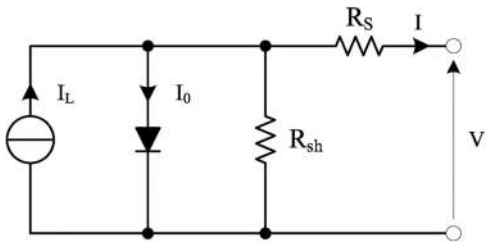

Fig. 3. Equivalent electrical circuit in the 5-parameter model.

adding a beam, diffuse and reflected radiation components on the tilted surface with a β the inclination angle. All tilted surface radiation models use the same techniques for projecting the beam and ground reflected radiation onto a tilted surface; they differ only in the estimate of diffuse radiation on a tilted surface. The contribution of beam radiation on a tilted surface (in short time intervals) can be calculated by using the geometric factor R_b [30], as shown in Eq. (3):

$$R_b = \frac{\cos\theta}{\cos\theta_z} \tag{3}$$

where

$$\cos\theta = \cos\theta_z\cos\beta + \sin\theta_z\cos(\gamma_{so} - \gamma_{su}) \tag{4}$$

In Eq. (4), β is the slope of the surface defined as the angle between the surface and the horizontal, while γ_{su} is the surface azimuth or the angle between the projection of the normal to the surface into the horizontal plane and the local merid. The sign convention for surface azimuth is identical to that for solar azimuth (zero facing equator, positive if west, negative if east). The slope is measured as a positive value when tilted in the direction of the azimuth specification.

The direct solar radiation on the tilted surface G_{bT} can be calculated by means of Eq. (5) starting from the beam radiation on the horizontal surface G_b.

$$G_{bT} = G_b \cdot R_b \tag{5}$$

The contribution of reflected radiation on a tilted surface G_{gT} is calculated by assuming the ground acts as an isotropic reflector. Defining R_r as the ratio of reflected radiation on a tilted surface to the total radiation on a horizontal surface, G_{bT} can be calculated using Eqs. (6) and (7):

$$R_r = 0.5(1 - \cos\beta)\rho_g \tag{6}$$

$$G_{gT} = G \cdot R_r \tag{7}$$

Where ρ_g is the ground reflectivity and G is the solar radiation on the horizontal surface.

The contribution of diffuse radiation on a tilted surface is determined by using the model developed by Perez et al. [31]. This model accounts for circumsolar, horizon brightening, and isotropic diffuse radiation by empirically derived "reduced brightness coefficients". The reduced brightness coefficients F_1' and F_2' are functions of sky clearness ε and sky brightness Δ parameters that can be calculated with Eqs. (8) and (9).

$$\varepsilon = \frac{\left[\frac{(G_d + G_{dn})}{G_d} + 1.041\theta_z^3\right]}{\left[1 + 1.041\theta_z^3\right]} \tag{8}$$

$$\Delta = m\frac{G_d}{G_{ex,n}} = \frac{G_d}{G_{ex}} \tag{9}$$

Where G_d is the diffuse radiation on the horizontal surface, G_{dn} is the direct normal beam radiation, G_{ex} is the extraterrestrial radiation and $G_{ex,n}$ is the extraterrestrial radiation at normal incidence.

To calculate the reduced brightness coefficients Eqs. (10) and (11) are utilized.

$$F_1' = F_{11}(\varepsilon) + F_{12}(\varepsilon)\cdot\Delta + F_{13}(\varepsilon)\cdot\theta_z \tag{10}$$

$$F_2' = F_{21}(\varepsilon) + F_{22}(\varepsilon)\cdot\Delta + F_{23}(\varepsilon)\cdot\theta_z \tag{11}$$

where θ_Z is in radians and the Perez coefficients (F_{11}, etc.) are given in Ref [31].

The tilted surface diffuse radiation G_{dT} can be estimated by the Eq. (13):

$$G_{dT} = G_d\left[0.5\left(1 - F_1'\right)(1 + \cos\beta) + F_1'\left(\frac{a}{c}\right) + F_2'\sin\beta\right] \tag{12}$$

Eq. (13) shows that the magnitude of the reduced brightness coefficients weighs the respective circumsolar, horizon brightening, and isotropic diffuse radiation components. The ratio a/c determines the angular location of the circumsolar region and can be calculated with Eq. (13).

$$\frac{a}{c} = \frac{\max[0, \cos\theta]}{\max[\cos(85°), \cos\theta_z]} \tag{13}$$

In general, the anisotropic sky models of Perez, et al. provide comparable estimates of the total radiation on a tilted surface and are recommended for general use.

Finally, the total radiation (G_T)incident on a tilted flat surface is reported in Eq. (14):

$$G_T = G_{bT} + G_{dT} + G_{gT} \tag{14}$$

2.1.2. Type 94: Photovoltaic array

This component models the electrical performance of a PV array and employs equations for an empirical equivalent circuit model (see Fig. 3) to predict the current-voltage characteristics of a single module. This circuit consists of a DC source, a diode and two resistors. The strength of the current source is dependent on solar radiation and the I-V characteristics of the diode are temperature-dependent. The results for a single module equivalent circuit are extrapolated to predict the performance of a multi-module array. For crystalline modules (either single crystal or polycrystalline technology), Type 94 employs an equivalent electrical circuit model involving five mathematical parameters. The component will determine these values from manufacturers' catalog data. Type 94 also includes an optional incidence angle modifier correlation to calculate how the reflectance of the PV module surface varies with the angle of incidence of solar radiation. Other outputs include current and voltage at the maximum power point along the IV curve, open-circuit voltage, and short circuit current.

2.1.2.1. Mathematical description (5-parameter model). The 5-parameter model is used to simulate dynamically the PV performance as a function of the incident solar radiation and air temperature [32]. This model permits the evaluation of the electrical performance of the PV cell modifying instantaneously the I-V characteristic curve of the PV cell from the reference to the actual conditions. It is based on an equivalent electrical circuit containing one diode, one ideal current generator and two electrical resistors.

The performance of the PV generator is determined by solving the equivalent electrical circuit shown in Fig. 3, which consists of the use of five parameters providing a direct/ideal current generator, a diode and two resistors. The five parameters are the photocurrent I_L, the diode reverse saturation current I_0, the empirical PV curve-fitting parameter γ, the series resistance R_s and the shunt resistance R_{sh}. These values are empirical and are not directly ascertained through physical measurements. Type 94 computes these values utilizing data extracted from the manufacturer's catalog.

The current-voltage equation for the equivalent circuit in Fig. 3 is represented by the Eq. (15):

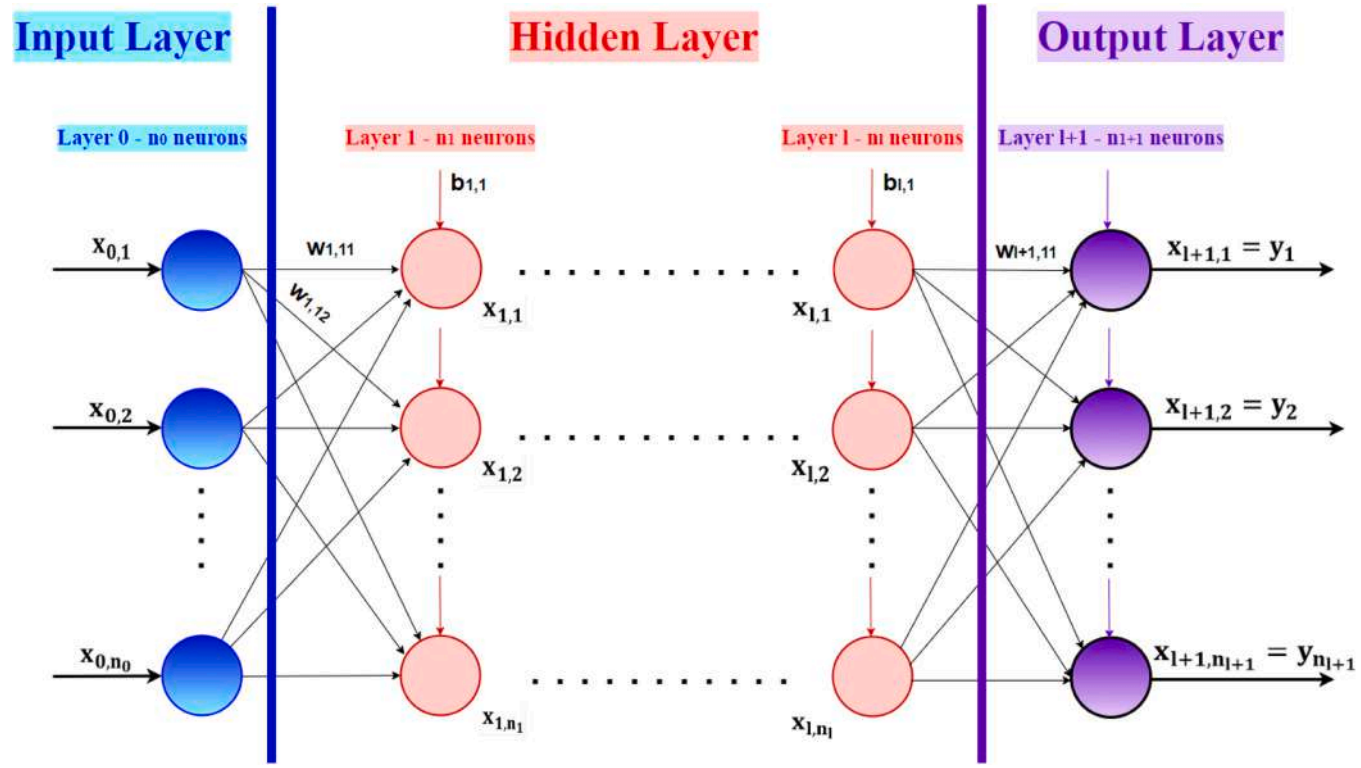

Fig. 4. Representation of an artificial neural network with n_0 inputs, n_{l+1} outputs and l hidden layer.

Table 1
ANN activation functions.

Name	Function	Equation	Codomain	Graph
Linear transfer function	purelin(x)	x	(-∞, +∞)	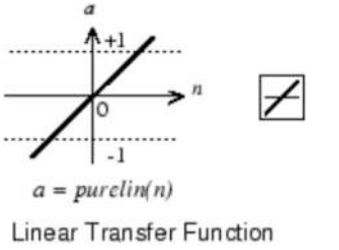
Log-sigmoid transfer function	logsig(x)	$\frac{1}{1+e^{-x}}$	(0, 1)	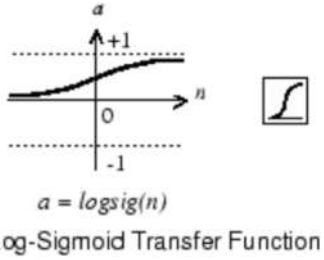
Hyperbolic tangent sigmoid transfer function	tansig(x)	$\frac{2}{1+e^{-2x}}-1$	(-1,1)	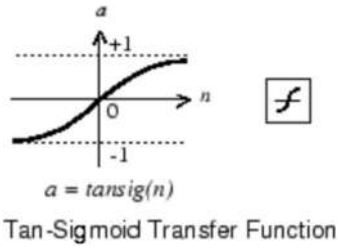

Table 2
PV module parameters at reference conditions [45–50].

Name	Cells	V_{oc} (V)	I_{sc} (A)	$V_{mp,ref}$ (V)	$I_{mp,ref}$ (A)	NOCT (K)	A (m^2)	μ_{Isc} (%/°C)	μ_{Voc} (%/°C)	$P_{pv,n}$ (W)	η_m (%)
TRAINING											
CanadianSolar290	60	38.50	9.72	31.60	9.18	316.15	1.64	0.050	-0.29	290.09	17.72
Jakson250	72	44.50	7.45	35.90	6.97	320.15	1.62	0.040	-0.32	250.22	12.88
LG300	60	40.10	9.65	32.90	9.15	318.15	1.64	0.030	-0.28	301.04	16.23
Panasonic330	96	69.70	6.07	58.00	5.70	317.15	1.67	0.034	-0.16	330.60	19.70
Suntech250	60	37.40	8.63	30.70	8.15	318.15	1.63	0.050	-0.34	250.21	15.40
TallMax320	72	45.80	9.10	37.10	8.63	317.15	1.94	0.050	-0.32	320.17	16.50

$$I = I_L - I_0\left[\exp\left(\frac{q}{\gamma k T_c}V + IR_s\right) - 1\right] - \frac{V + IR_s}{R_{sh}} \tag{15}$$

Where k is the Boltzmann constant and Tc is the cell temperature.

The insolation and temperature dependence of the PV module is given by using Eqs. (16) and (17):

$$I_L = I_{L,ref}\ \frac{G_T}{G_{T,ref}} \tag{16}$$

$$\frac{I_0}{I_{0,ref}} = \left(\frac{T_c}{T_{c,ref}}\right)^3 \tag{17}$$

Herafter, equations used to find the 5 parameters in the reference conditions are described. Fry [33] has shown that the negative reciprocal of the short-circuit IV slope closely approximates the shunt resistance:

$$R_{sh} \cong \frac{-1}{\left(\frac{dI}{dV}\right)_{V=0}} \tag{18}$$

This expression reduces the number of unknown quantities to four: $I_{L,ref}$, $I_{o,ref}$, γ, and R_s. Rearranging Eq. (15) (and neglecting the "-1") at open-circuit *oc*, short-circuit *sc*, and maximum power *mp* conditions yields, the following expressions for $I_{L,ref}$, $I_{o,ref}$, γ:

$$I_{L,ref} = I_{sc,ref}\ \left(1 + \frac{R_s}{R_{sh}}\right) \tag{19}$$

$$I_{0,ref} = \frac{I_{L,ref} - \frac{V_{oc,ref}}{R_{sh}}}{\exp\left(\frac{q}{\gamma k T_{c,ref}} - V_{oc,ref}\right)} \tag{20}$$

$$\gamma = \frac{\left(q\left(V_{mp,ref} - V_{oc,ref} + I_{mp,ref}\ R_s\right)\right)}{kT_{c,ref}\ln\left(\frac{I_{L,ref} - I_{mp,ref} - \frac{V_{mp,ref} + I_{mp,ref}\ R_s}{R_{sh}}}{I_{sc,ref} - \frac{V_{oc,ref}}{R_{sh}}}\right)} \tag{21}$$

Where q is the electron charge constant.

The fifth equation is derived by taking the analytical derivative of voltage with respect to temperature at the reference open-circuit condition. This analytical value is matched to the open-circuit temperature coefficient, a catalog specification. Differentiating Eq. (15) with respect to temperature at the open-circuit condition yield, Eq. (22) is obtained:

$$\frac{\partial V_{oc}}{\partial T_c} = \mu_{Voc} = \frac{\mu_{Isc} - \frac{I_{0,ref}}{T_c}\left(3 + \frac{q\varepsilon}{\frac{\gamma}{N_{cs}}kT}\right)\exp\left(\frac{q}{k\gamma T_{c,ref}}\right)}{\frac{q}{k\gamma T_{c,ref}}I_{0,ref}\exp\left(\frac{q}{k\gamma T_{c,ref}}V_{oc,ref}\right) + \frac{1}{R_{sh}}} \tag{22}$$

Where N_{cs} is the number of cells in series.

Type 94 uses an iterative search routine in these four equations to calculate the equivalent circuit characteristics, which provides the values of $I_{L,ref}$, $I_{0,ref}$, $R_{s,ref}$, R_{sh} and a_{ref}. To solve the equation system, an iterative search routine is used to find the correct values for R_s and γ by matching the analytical value for the temperature coefficient of open-circuit voltage μ_{Voc} to that given in the catalog.

As previously shown in Eqs. (16) and (17), the parameter values under operating conditions are obtained by updating the I_L and I_0 values, as a function of solar radiation absorbed and the cell temperature, respectively. The latter is calculated using the Nominal Operating Cell Temperature (NOCT). In this way, the characteristic curve is updated at each time instant as a function of the cell temperature and the solar radiation absorbed [34]. In addition, absorbed solar power is evaluated considering the Incidence Angle Modifier (IAM) [35].

The electric PV power produced is calculated at the maximum power point of the characteristic curve by Eq. (23):

$$P_{pv}(t) = I_{mp}(t)\cdot V_{mp}(t) \tag{23}$$

MPPT relies on a control system designed to optimize the operation of a PV system by maintaining it in the most effective conditions for maximum power output [36].

2.1.2.2. Module opeating temperature. Type 94 uses temperature data from the standard NOCT measurements to compute the module temperature T_c at each time step. The NOCT temperature ($T_{c,NOCT}$) is the operating temperature of the module with a wind speed of 1 m/s, no electrical load, and certain specified insolation and ambient temperature [37]. The values for insolation $G_{T,NOCT}$ and ambient temperature $T_{a,NOCT}$ are usually 800 W/m^2 and 20° C. Type 94 uses the NOCT data to determine the ratio of the module transmittance-reflectance product to the module loss coefficient:

$$\frac{\tau\alpha}{U_L} = \frac{\left(T_{c,NOCT} - T_{a,NOCT}\right)}{G_{T,NOCT}} \tag{24}$$

Assuming that this ratio is constant, the module temperature at any time step is:

$$T_C = T_a\ \frac{\left(1 - \frac{\eta_m}{\tau\alpha}\right)}{\left(\frac{G_T\tau\alpha}{U_L}\right)} \tag{25}$$

where η_m is the conversion efficiency of the module, U_L is the PV thermal loss coefficient and τα may be either a constant or a value calculated from an incidence angle correlation, as described in Section 2.1.2.3.

2.1.2.3. Incidence angle modifier correlation. Type 94 includes an optional "incidence angle modifier" routine. If this routine is used, an empirical correlation determines the transmittance-reflectance product (τα) of the module at each time step. This calculation is based on the module slope, and the angle of incidence and intensity of each radiation component (direct, diffuse, and ground-reflected). For most locations, a given PV array will generate about 10% less energy over a year when the incidence angle routine is enabled. τα at normal incidence is not usually included in the list of manufacturer's parameters, although 0.9 is usually a good estimate. The expression for the incidence angle modifier, taken

Locality	Country	Group		Sub-group	Lat. (°)	Long. (°)	Alt. (m)	Training T Validation V
Toamasina	Madagascar	A Tropical/ megathermal climates	Af	Tropical rainforest climate	-18.1	49.4	6	T
Singapore	Singapore				1.0	104.0	16	V
Recife, Pernambuco	Brazil		Am	Tropical monsoon climate	-8.1	-34.8	19	T
Miami, Florida	United States				25.8	-80.3	2	V
Lihue, Hawaii	United States		As	Tropical savanna climate with dry-summer	22.0	-159.3	45	T
Mombasa	Kenya				-4.0	39.6	57	V
Caracas	Venezuela		Aw	Tropical savanna climate with dry-winter	10.6	-67.0	43	T
Kano	Nigeria				12.0	8.5	481	V
Baghdad	Iraq	B Dry (desert and semi-arid) climates	BWh	Hot desert climate	33.3	44.4	33	T
Cairo	Egypt				31.8	31.3	36	V
Kabul	Afghanistan		BSk	Cold semi-arid (steppe) climate	34.5	69.2	1791	T
Baku	Azerbaijan				40.4	49.8	5	V
Odessa, Texas	United States		BSh	Hot semi-arid (steppe) climate	46.5	-102.4	42	T
Maracaibo	Venezuela				10.6	-71.6	40	V
Buenos Aires	Argentina	C Temperate/mesothermal climates	Cfa	Humid subtropical climates	-34.6	-58.5	24	T
Milan	Italy				45.6	8.7	211	V
Berlin	Germany		Cfb	Oceanic climate, Marine west coast climate	52.5	13.4	50	T
London	United Kingdom				51.5	-0.1	77	V
Vancouver, British Columbia	Canada				49.2	-123.2	87	T
Melbourne, Victoria	Australia				-37.8	145.0	38	V
Bogotá, Cundinamarca	Colombia		Cfb	Oceanic climate, Subtropical highland climate with uniform rainfall	4.05	-74.1	2548	T
Wellington	New Zealand				-41.3	174.8	6	V
Reykjavík	Iceland		Cfc	Subpolar oceanic climates	64.1	-21.9	66	T
Auckland Islands	New Zealand				-37.0	174.8	6	V
Rome	Italy		Csa	Hot-summer Mediterranean climate	41.8	12.6	131	T
Adelaide	Australia				-34.9	138.5	4	V
Porto	Portugal		Csb	Warm-summer Mediterranean climate	41.1	-8.6	100	T
La Coruna	Spain				43.4	-8.4	67	V
New Delhi	India		Cwa	Monsoon-influenced humid subtropical climate	28.6	77.2	212	T
Hong Kong	China				22.3	114.2	62	V
Johannesburg	South Africa		Cwb	Subtropical highland climate	-26.1	28.2	1692	T
Nairobi	Kenya				-1.15	36.9	1624	V
Bucharest	Romania	D Continental/microthermal climates	Dfa	Hot-summer humid continental climate	44.5	26.2	91	T
Toronto, Ontario	Canada				43.7	-79.2	157	V
Moskva	Russia		Dfb	Warm-summer humid continental climate	55.8	37.6	156	T
Ottawa, Ontario	Canada				45.4	-75.7	79	V
Tromsø	Norwey		Dfc	Subarctic climate	69.6	18.9	102	T
Anchorage, Alaska	United States				61.2	-150.0	35	V
Oymyakon, Sakha Republic	Russia		Dfd	Extremely cold subarctic climate	63.3	143.1	740	T
Verhojansk, Sakha Republic	Russia				67.5	133.4	137	V
Hakkâri	Turkey		Dsa	Hot, dry-summer continental climate	37.6	43.8	1720	T
Cambridge Bay, Nunavut	Canada				69.1	-105.1	23	V
Dras	India		Dsb	Warm, dry-summer continental climate	34.4	75.8	3100	T
Flagstaff, Arizona	United States				35.1	-111.7	2135	V
Beijing	China		Dwa	Monsoon-influenced hot-summer humid continental climate	39.93	116.3	55	T
Seoul	South Korea				37.6	127.0	86	V
Pyongyang	North Korea		Dwb	Monsoon-influenced warm-summer humid continental climate	39.0	125.8	35	T
Vladivostok	Russia				43.1	131.9	80	V

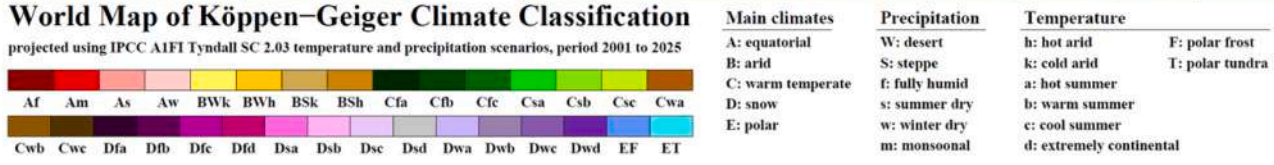

Fig. 5. Localities belonging to the training and validation set along with the Koppen climate classification.

Table 3
Yearly average and standard deviation values of external air temperature and horizontal global solar radiation.

Locality	$T_{ae,avg}$ (°C)	G_{avg} (W/m^2)	$T_{ae,sd}$ (°C)	G_{sd} (W/m^2)	Optimal PV angle (°)
Toamasina	23.30	205.87	3.59	287.75	-16
Singapore	26.62	185.30	2.46	264.60	2
Recife, Pernambuco	28.58	241.68	2.78	324.87	-4
Miami, Florida	24.31	204.69	4.28	279.76	26
Lihue, Hawaii	23.92	207.60	2.63	278.78	20
Mombasa	26.15	227.54	3.26	310.19	0
Caracas	25.98	184.66	2.84	263.84	10
Kano	26.29	256.41	6.18	335.16	16
Baghdad	20.12	238.15	10.11	316.64	32
Cairo	21.32	231.37	6.53	308.61	28
Kabul	12.06	217.73	10.58	302.55	34
Baku	14.57	152.41	9.42	235.40	28
Odessa, Texas	10.16	141.77	9.47	219.53	34
Maracaibo	27.54	179.50	3.41	258.76	10
Buenos Aires	17.42	194.89	5.89	277.42	-28
Milan	11.62	135.71	8.94	208.70	36
Berlin	9.42	114.35	8.53	184.79	38
London	10.78	105.50	5.79	174.31	36
Vancouver, British Columbia	9.84	143.96	5.83	224.71	36
Melbourne, Victoria	14.00	175.04	5.82	257.19	-30
Bogotá, Cundinamarca	13.26	193.15	4.03	283.51	2
Wellington	13.51	160.44	4.32	243.43	-32
Reykjavík	4.37	89.35	5.31	151.59	44
Auckland Islands	15.09	175.10	4.12	255.73	-30
Rome	15.21	178.21	7.19	254.13	36
Adelaide	16.65	204.08	6.14	288.89	-28
Porto	14.48	178.22	5.30	258.44	34
La Coruna	14.09	139.92	4.12	215.45	32
New Delhi	25.07	225.08	7.87	299.22	32
Hong Kong	22.87	162.66	5.51	243.38	20
Johannesburg	15.47	235.95	6.04	318.23	-26
Nairobi	19.23	211.37	4.19	299.92	4
Bucharest	10.58	151.24	10.07	229.83	34
Toronto, Ontario	7.37	160.65	10.99	238.66	36
Moskva	5.01	109.72	11.05	180.47	42
Ottawa, Ontario	5.93	157.26	12.46	230.58	40
Tromsø	2.95	72.47	6.61	129.23	46
Anchorage, Alaska	2.64	101.62	9.77	165.48	48
Oymyakon, Sakha Republic	-16.15	122.17	24.05	188.72	52
Verhojansk, Sakha Republic	-15.05	109.11	23.73	174.86	52
Hakkâri	10.11	196.29	11.16	284.34	30
Cambridge Bay, Nunavut	-14.56	113.79	16.11	183.37	52
Dras	2.09	186.47	12.50	275.34	30
Flagstaff, Arizona	7.30	213.52	9.81	289.17	36
Beijing	11.79	148.15	11.76	219.17	38
Seoul	11.84	138.57	10.83	211.44	34
Pyongyang	9.58	146.57	11.95	218.39	36
Vladivostok	4.27	150.77	12.15	217.14	44

from King et. al [35] is:

$$IAM = 1 - \left(1.098\cdot10^{-4}\right)\theta - \left(6.267\cdot10^{-6}\right)\theta^2 + \left(6.583\cdot10^{-7}\right)\theta^3 - \left(1.4272\cdot10^{-8}\right)\theta^4 \quad (26)$$

Where, in this case θ is the angle of incidence in degrees, with θ = 0 indicating normal incidence.

The angle of incidence for the beam component of the solar radiation is obtained directly as an output from the Type 15 Solar Radiation Processor. However, Type 15 does not calculate effective angles of incidence for the diffuse and ground-reflected radiation components. Type 94 uses two additional correlations to find these effective angles of incidence. These correlations, developed by Duffie and Beckman [37], are:

$$\theta_{eff,diff} = 59.7 - 0.1388\cdot\beta + 0.001497\cdot\beta^2 \quad (27)$$

$$\theta_{eff,gnd} = 90 - 0.5788\cdot\beta + 0.002693\cdot\beta^2 \quad (28)$$

The total insolation on the array is found by summing the individual radiation components and multiplying them by their appropriate incidence angle modifiers:

$$G_{T,eff} = \tau\alpha_{norm}\left(G_{T,beam}IAM_{beam} + G_{T,diff}IAM_{diff} + + G_{T,gnd}IAM_{gnd}\right) \quad (29)$$

2.2. Artificial neural network

The components of an ANN can be listed as (i) input layer, (ii) hidden layer(s), (iii) output layer, (iv) weights and biases between layers and (v) activation function [38]. A generalized representation of an ANN can be seen in Fig. 4.

There are several types of activation functions in the literature; the most commonly used are reported in Table 1.

Each ANN layer includes neurons like our brains, which are the core processing units of the ANNs. The output of the ANN with l hidden layer can be expressed in a matrix form:

$$x_{l+1} = y = \varphi(w_{l+1}x_l + b_{l+1}) \quad (30)$$

Where x_{l+1} is the output y from the ANN, b_{l+1} is the bias vector of the output layer and w_{l+1} represents the weight matrix between the l-th hidden layer and the output layer. The training phase foresees the determination of the weights between the different layers of the ANN. The optimal weights are determined by an optimization routine that minimizes the errors between the ANN output value and the target values used to train the ANN [39,40]. Initial simulations indicated that both the Bayesian and LM algorithms yielded comparable results, exhibiting a disparity of merely 0–1% in accuracy metrics. This phenomenon stems from the limited input variables, the singular output, and the extensive dataset utilized during the training phase to elucidate the input-output correlation.

The algorithms used in this work are related to the Deep Learning Toolbox [41]. The ANN architecture can be optimized by identifying the optimal number of neurons that maximize the accuracy, by using some common accuracy metrics [42]. On the basis, of the optimal architecture, a sensitivity analysis of the optimal ANN model was conducted using Garson's algorithm illustrated, in his reference [43], for the case with two input neurons, one hidden layer with two neurons and one output neuron. The method quantitatively demonstrates the importance of each input in predicting each output, namely to determine the influence of each input variable and its contribution to the output. This method is also used to eliminate irrelevant input; namely, the most significant explanatory variables are determined, and then the variables below a fixed threshold are excluded from the ANN. This allows the ANN size to be reduced and thus minimizes redundancy in the training data.

The same method was illustrated by Gevrey et al. [44], called the weight method, considering the ANN with three input neurons, one hidden layer with four neurons and one output neuron.

In this paper, a generalized procedure of the Garson method is proposed. To determine the relative importance of each input to each

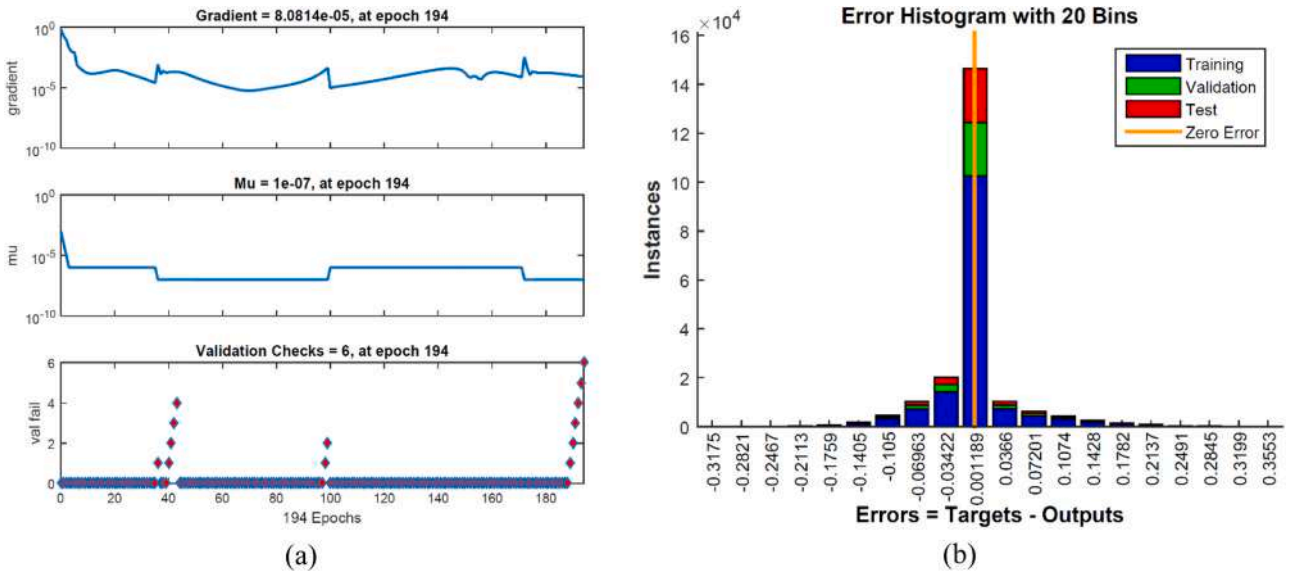

Fig. 6. ANN with 7 neurons in the hidden layer for the Jakson photovoltaic module (a) training state and (b) histogram of errors divided into training, validation, and testing data.

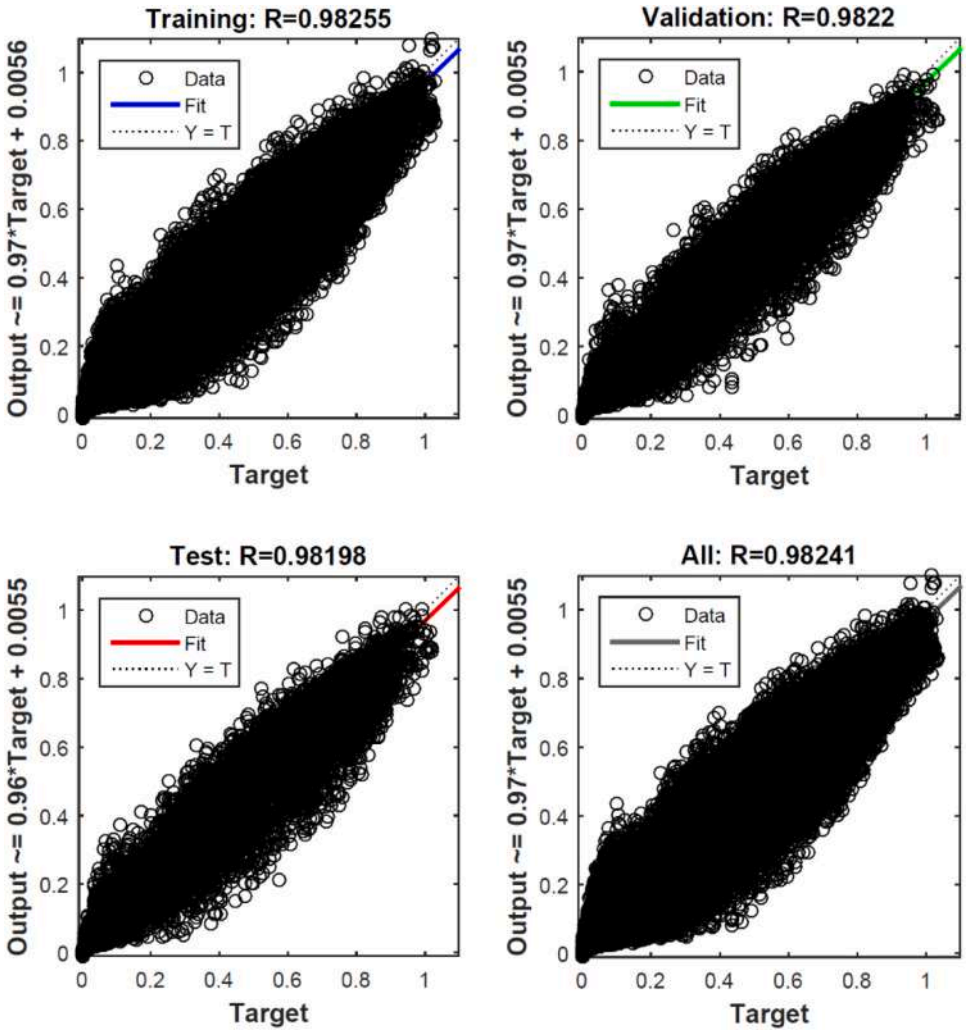

Fig. 7. Regression diagram for the training, validation, testing and overall processes of the ANN with 7 neurons in the hidden layer for the Jakson photovoltaic module.

Table 4
RMSE, R^2 and MAE values as a function of the number of neurons in the hidden layer for the different photovoltaic modules.

	Neurons	RMSE (-)	R^2 (-)	MAE (-)	RMSE increase (%)	R^2 increase (%)	MAE increase (%)
CanadianSolar290	1	0.0521	0.9559	0.0311			
	2	0.0480	0.9626	0.0267	-7.91	0.70	-14.24
	3	0.0471	0.9640	0.0241	-1.90	0.15	-9.68
	4	0.0470	0.9642	0.0234	-0.24	0.02	-3.20
	5	0.0468	0.9645	0.0230	-0.45	0.03	-1.59
	6	0.0467	0.9646	0.0229	-0.14	0.01	-0.17
	7	**0.0465**	**0.9649**	**0.0226**	**-0.40**	**0.03**	**-1.52**
	8	0.0466	0.9648	0.0228	0.09	-0.01	0.87
	9	0.0465	0.9649	0.0228	-0.07	0.01	-0.14
	10	0.0465	0.9649	0.0225	-0.02	0.00	-0.93
Jakson250	1	0.0526	0.9556	0.0315			
	2	0.0482	0.9627	0.0269	-8.32	0.74	-14.49
	3	0.0473	0.9641	0.0243	-1.93	0.15	-9.66
	4	0.0471	0.9644	0.0234	-0.34	0.03	-3.64
	5	0.0470	0.9645	0.0234	-0.25	0.02	-0.13
	6	0.0468	0.9648	0.0230	-0.31	0.02	-1.81
	7	**0.0466**	**0.9651**	**0.0225**	**-0.53**	**0.04**	**-2.14**
	8	0.0467	0.9650	0.0225	0.18	-0.01	-0.09
	9	0.0467	0.9650	0.0228	-0.03	0.00	1.42
	10	0.0466	0.9652	0.0227	-0.23	0.02	-0.51
LG300	1	0.0537	0.9522	0.0325			
	2	0.0484	0.9612	0.0275	-9.92	0.95	-15.33
	3	0.0467	0.9638	0.0232	-3.44	0.27	-15.70
	4	0.0466	0.9640	0.0227	-0.32	0.02	-2.27
	5	0.0467	0.9639	0.0233	0.23	-0.02	2.52
	6	0.0464	0.9643	0.0230	-0.61	0.05	-1.20
	7	**0.0463**	**0.9645**	**0.0227**	**-0.18**	**0.01**	**-1.41**
	8	0.0463	0.9644	0.0230	0.07	-0.01	1.51
	9	0.0463	0.9645	0.0227	-0.15	0.01	-1.38
	10	0.0463	0.9644	0.0227	0.16	-0.01	-0.15
Panasonic330	1	0.0502	0.9605	0.0294			
	2	0.0462	0.9664	0.0231	-7.85	0.62	-21.40
	3	0.0462	0.9665	0.0233	-0.12	0.01	0.76
	4	0.0461	0.9666	0.0229	-0.09	0.01	-1.86
	5	0.0460	0.9667	0.0228	-0.24	0.02	-0.49
	6	0.0458	0.9670	0.0225	-0.44	0.03	-1.10
	7	0.0458	0.9670	0.0224	-0.03	0.00	-0.61
	8	**0.0456**	**0.9673**	**0.0220**	**-0.32**	**0.02**	**-1.50**
	9	0.0457	0.9672	0.0222	0.14	-0.01	0.74
	10	0.0456	0.9673	0.0219	-0.21	0.01	-1.26
Suntech250	1	0.0521	0.9563	0.0310			
	2	0.0481	0.9627	0.0266	-7.56	0.66	-14.09
	3	0.0473	0.9639	0.0241	-1.69	0.13	-9.24
	4	0.0472	0.9641	0.0234	-0.22	0.02	-3.24
	5	0.0471	0.9642	0.0234	-0.22	0.02	0.19
	6	**0.0468**	**0.9647**	**0.0226**	**-0.68**	**0.05**	**-3.28**
	7	0.0469	0.9646	0.0230	0.18	-0.01	1.78
	8	0.0468	0.9647	0.0229	-0.23	0.02	-0.72
	9	0.0468	0.9647	0.0228	0.03	0.00	-0.38
	10	0.0467	0.9648	0.0228	-0.17	0.01	-0.15
TallMax320	1	0.0518	0.9569	0.0308			
	2	0.0480	0.9630	0.0265	-7.34	0.64	-13.96
	3	0.0471	0.9643	0.0241	-1.88	0.13	-9.06
	4	0.0470	0.9645	0.0232	-0.21	0.02	-3.73
	5	0.0469	0.9646	0.0234	-0.21	0.01	0.86
	6	**0.0466**	**0.9651**	**0.0226**	**-0.64**	**0.05**	**-3.42**
	7	0.0467	0.9649	0.0230	0.21	-0.02	1.77
	8	0.0467	0.9650	0.0228	0.00	0.01	-0.87
	9	0.0466	0.9650	0.0227	-0.21	0.00	-0.44
	10	0.0466	0.9652	0.0227	0.00	0.02	0.00

output, the computation process is as follows:

(Step 1) Identification of all routes between $x_{0,i}$ and y_j through the neurons of the l hidden layers, for a couple constituted by a neuron of the input layer $x_{0,i}$ and a neuron of the output layer y_j. The number of routes between each couple $x_{0,i}$ and y_j is equal to the overall hidden neurons $N_R = n_1 + n_2 + .. + n_i + \ldots + n_l$.
(Step 2) Calculation of the r-th overall weight $W_{r,ij}$, namely the product of all absolute values of weights of a specific route r between the i-th input $x_{0,i}$ and the j-th output y_j:

$$W_{r,ij} = \prod_{k=1}^{l+1} |w_k| \tag{31}$$

This product is composed of $l+1$ weights $w_{k,ij}$; specifically, the number of weight connections needed corresponds to the quantity of connections required to transition from the input neuron to the output neuron. In addition, only one weight for each hidden layer appears in Eq. (31) as highlighted by subscript k.

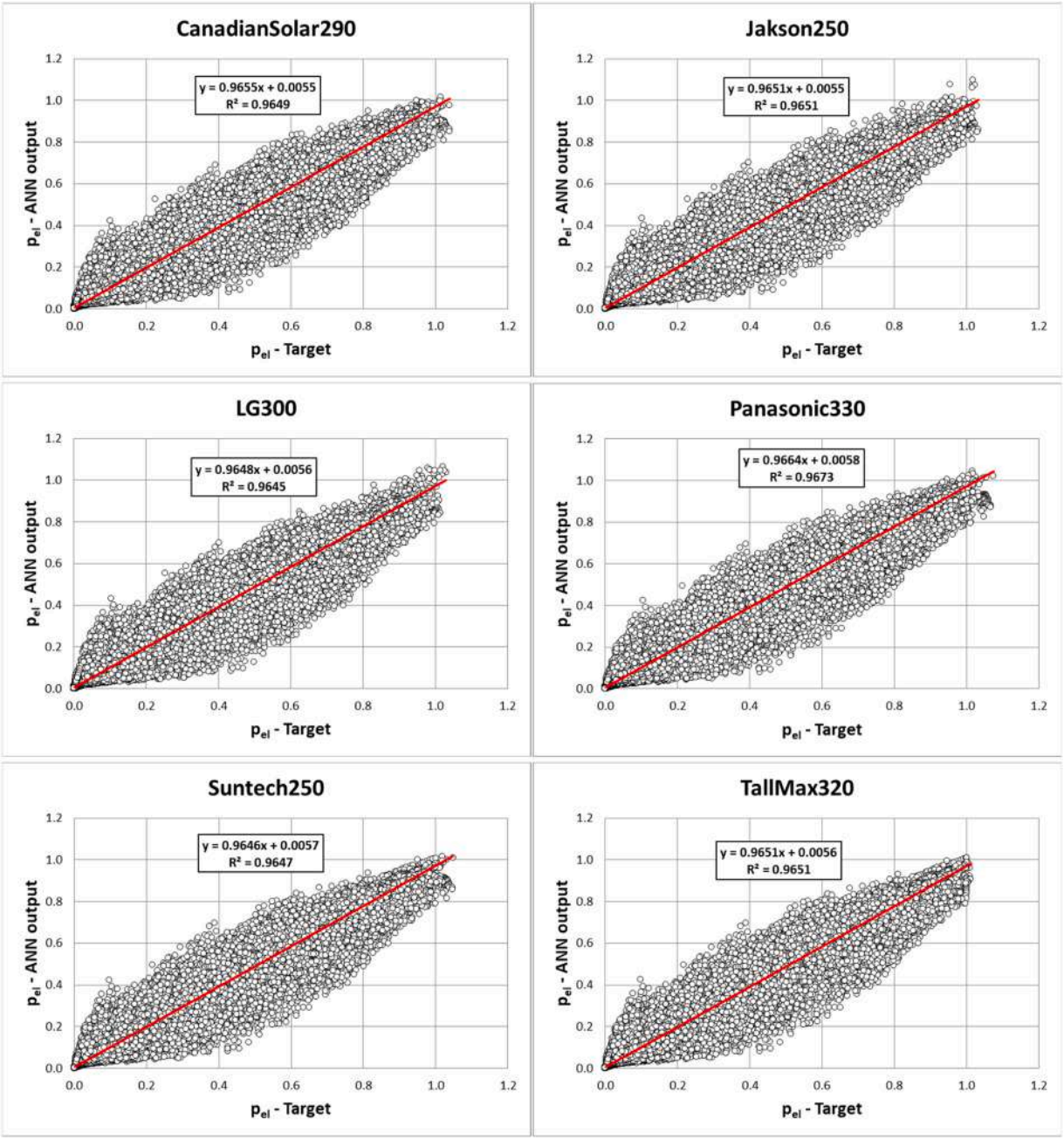

Fig. 8. Regression diagram between the target and output for the different optimal ANNs of the network.

(Step 3) Determination of the sum s_{ij} of the r overall weights $W_{r,ij}$, summed overall weights, between the i-th input $x_{0,i}$ and the j-th output y_j

$$s_{ij} = \sum_{r=1}^{N_R} W_{r,ij} \tag{32}$$

(Step 4) Application of Steps (1)-(3) for all $(n_0 \bullet n_{l+1})$ couples of input neurons-output neurons

(Step 5) Calculation of the percentage sensitivity index S_{ij} of each i-th input on the j-th output with the following equation:

$$S_{ij} = \frac{s_{ij}}{\sum_{i=1}^{n_0} s_{ij}} 100 \tag{33}$$

(Step 6) Repeat Steps (5) for the n_{l+1} output neurons.

3. Case study

In this section, data related to the different PV module and localities considered for the training and validation phase of the ANNs are extensively described.

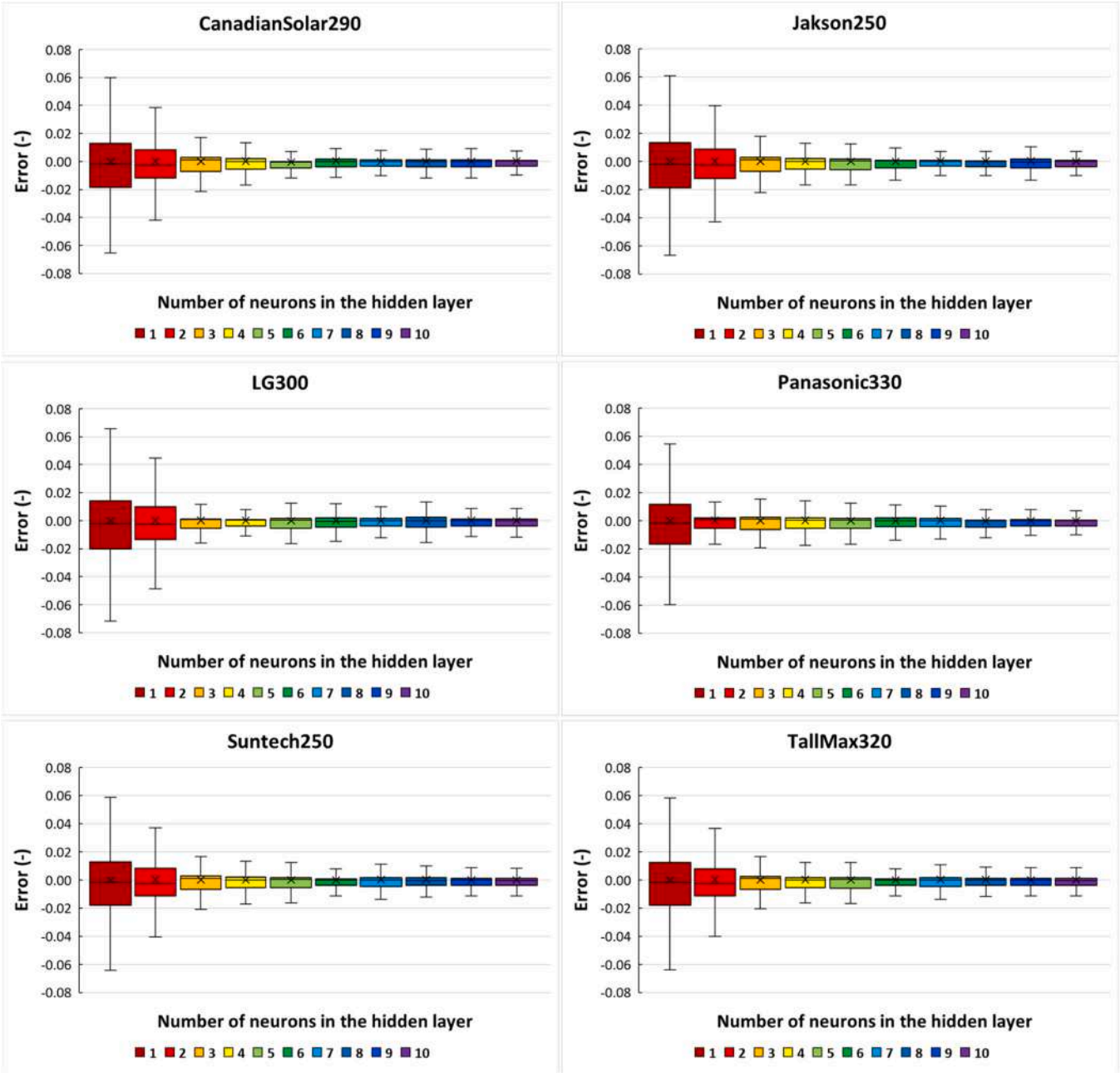

Fig. 9. Error boxplots of the dimensionless electrical power as a function of the number of neurons.

3.1. Photovoltaic modules

In total, eight PV modules were examined, and their electrical and thermal characteristics under reference conditions are detailed in Table 2.

The primary parameters for the PV module under reference conditions include: open-circuit voltage ($V_{oc,ref}$), short-circuit current ($I_{sc,ref}$), voltage at the maximum power point ($V_{mp,ref}$), current at the point of maximum power (I_{mp}), NOCT, module area A, temperature coefficient of short-circuit current (μ_{Isc}), temperature coefficient of open-circuit voltage (μ_{Voc}), nominal power ($P_{pv,n}$) obtained by multiplying voltage and current at the point of maximum power, and module efficiency (η_m). These values are provided by the manufacturer [45–50] and are essential for Type 94 in TRNSYS to calculate the power output using the 5-parameter model. Reference conditions are defined at a temperature of 25°C and solar radiation of 1000 W/m^2.

3.2. Climatic data

With the aim to provide a forecasting tool able to forecast PV performance in any climatic condition, different worldwide localities belonging to different climate zones were identified. In the first phase, 80 localities were selected. Successively, localities were reduced maintaining the general validity tool condition with the following rationale: (i) at least two localities for each Koppen climate sub-group [51–53] (as shown in Fig. 5); (ii) the choice of localities has to determine a uniform distribution of localities in the different continents and latitudes based on the continent's size and population; (iii) the choice of localities has to lead to climatic conditions very different with very and low sunny localities, very hot and cold localities and very and low windy localities (as shown in the Table 3).

Consequently, in order to enhance the versatility and adaptability of the ANNs to various locations, 48 sites representing diverse climate groups in the Köppen classification, each characterized by distinct

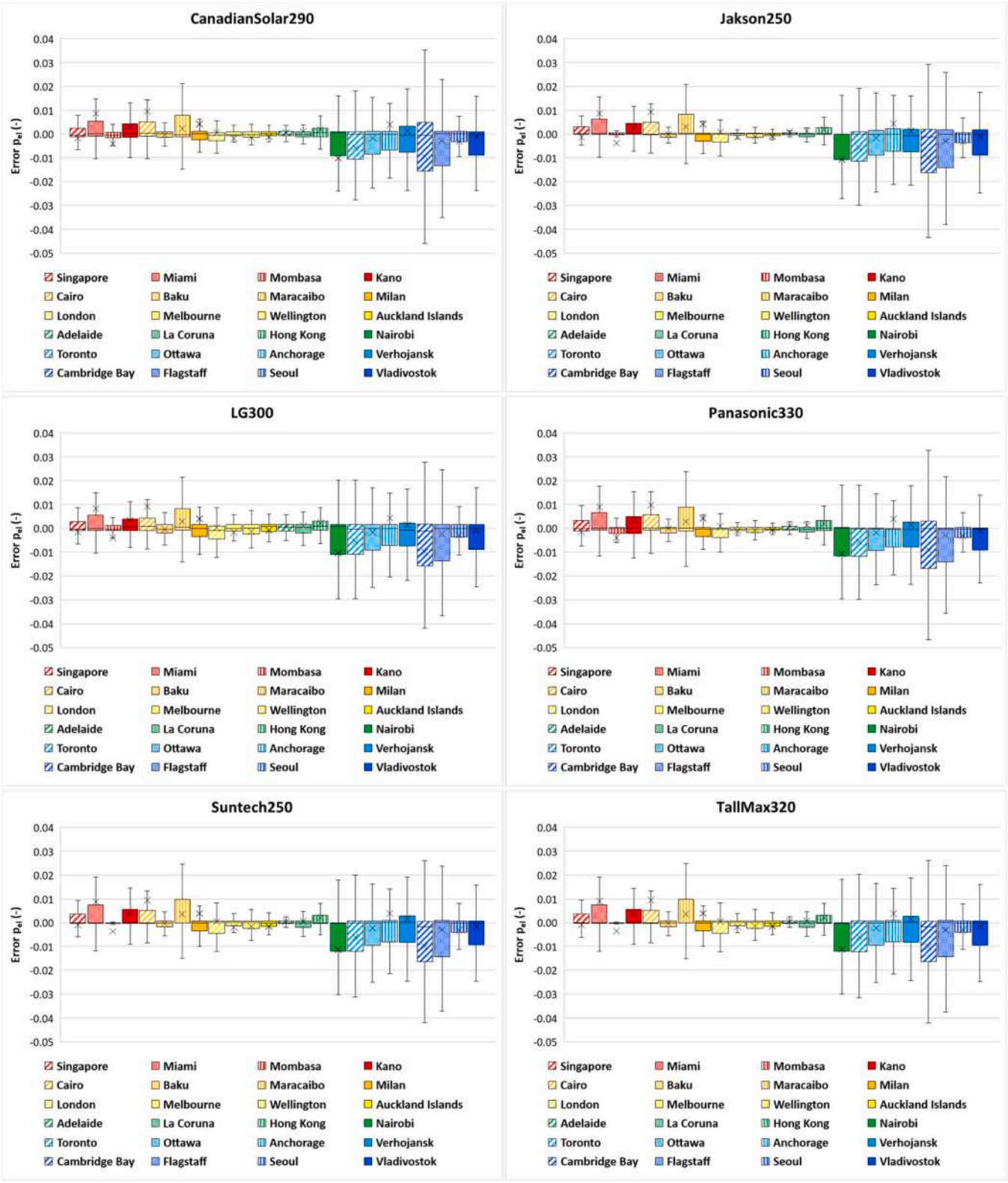

Fig. 10. Dimensionless electrical hourly power error boxplots using the ANNs in the 24 localities of the validation dataset.

climates, were taken into account [51–53]. Specifically, two locations were considered for each climate subgroup, except for the Cfb subgroup, which encompasses four locations. Fig. 5 illustrates the 48 locations examined in this study.

For each location, the TRNSYS library provides known hourly values of air temperature and horizontal solar radiation in a typical year tm2 file. Yearly average and standard deviation values of external air temperature, $T_{ae,avg}$ and $T_{ae,sd}$, and horizontal global solar radiation, G_{avg} and G_{sd}, are provided in Table 3. In addition, the table provided the optimal tilt angle associated with the maximum PV electricity for each locality.

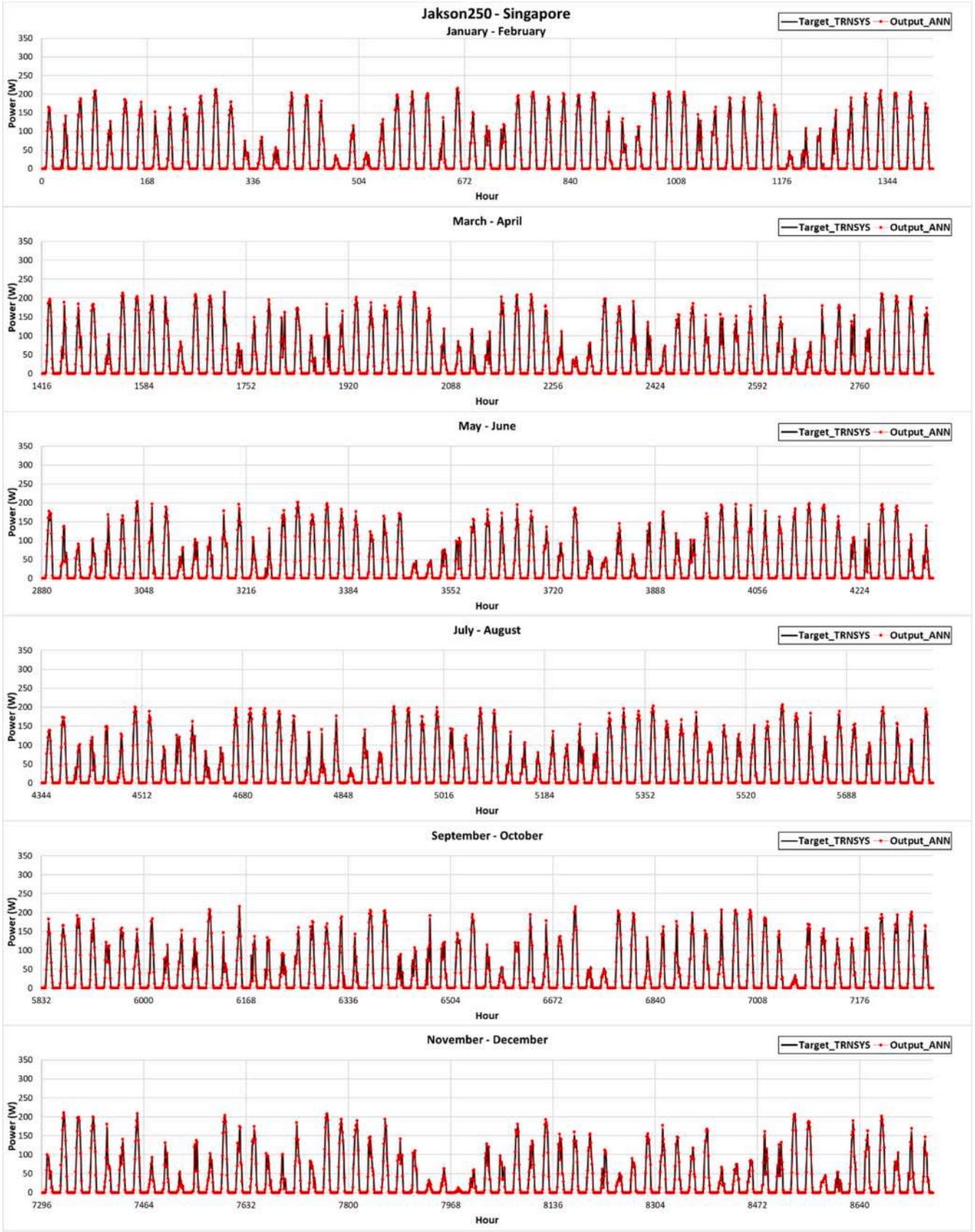

Fig. 11. Hourly trend throughout the year of the electrical energy produced by the Jakson250 PV module in Singapore calculated with TRNSYS and with the ANN.

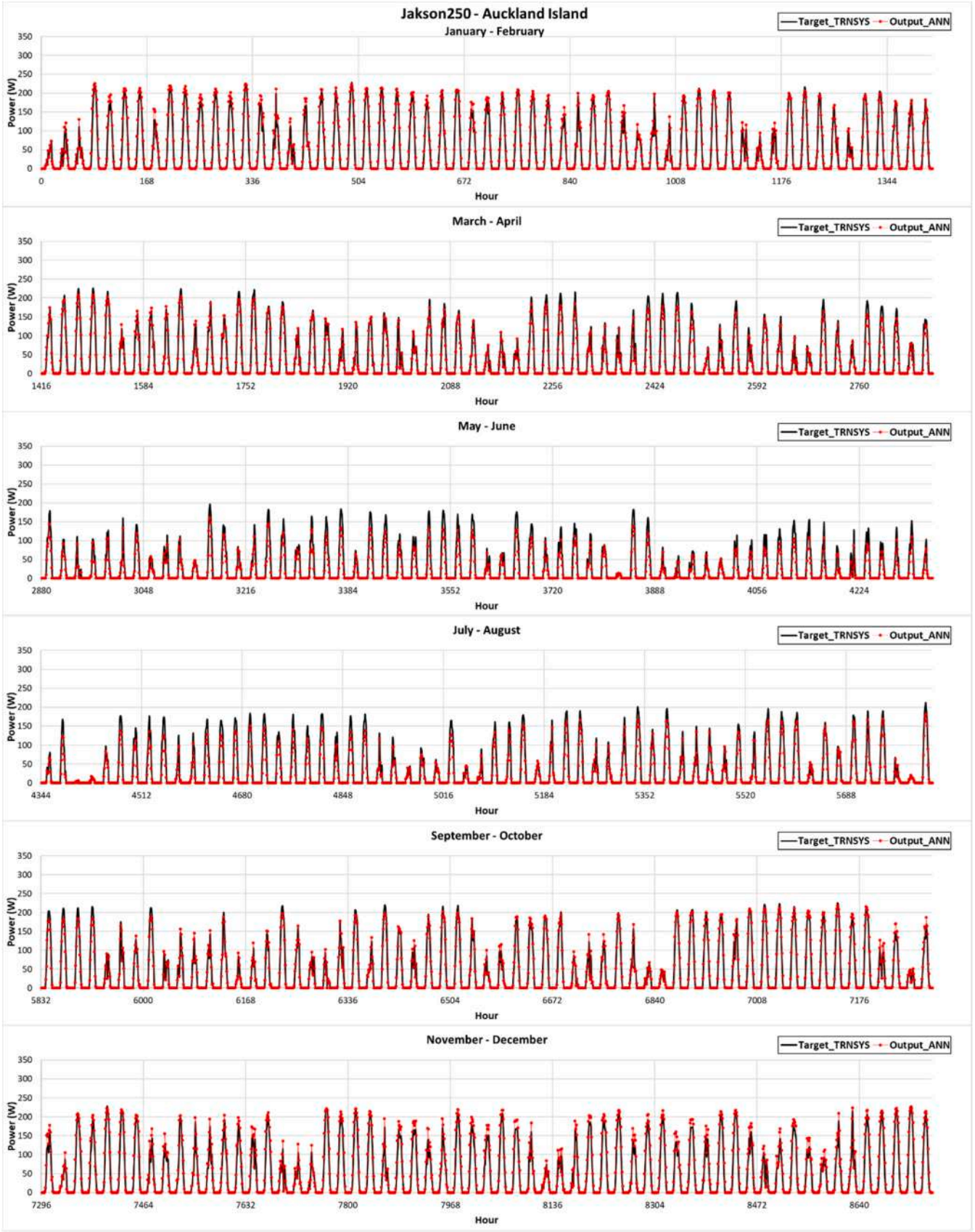

Fig. 12. Hourly trend throughout the year of the electrical energy produced by the Jakson250 PV module in Auckland Island calculated with TRNSYS and with the ANN.

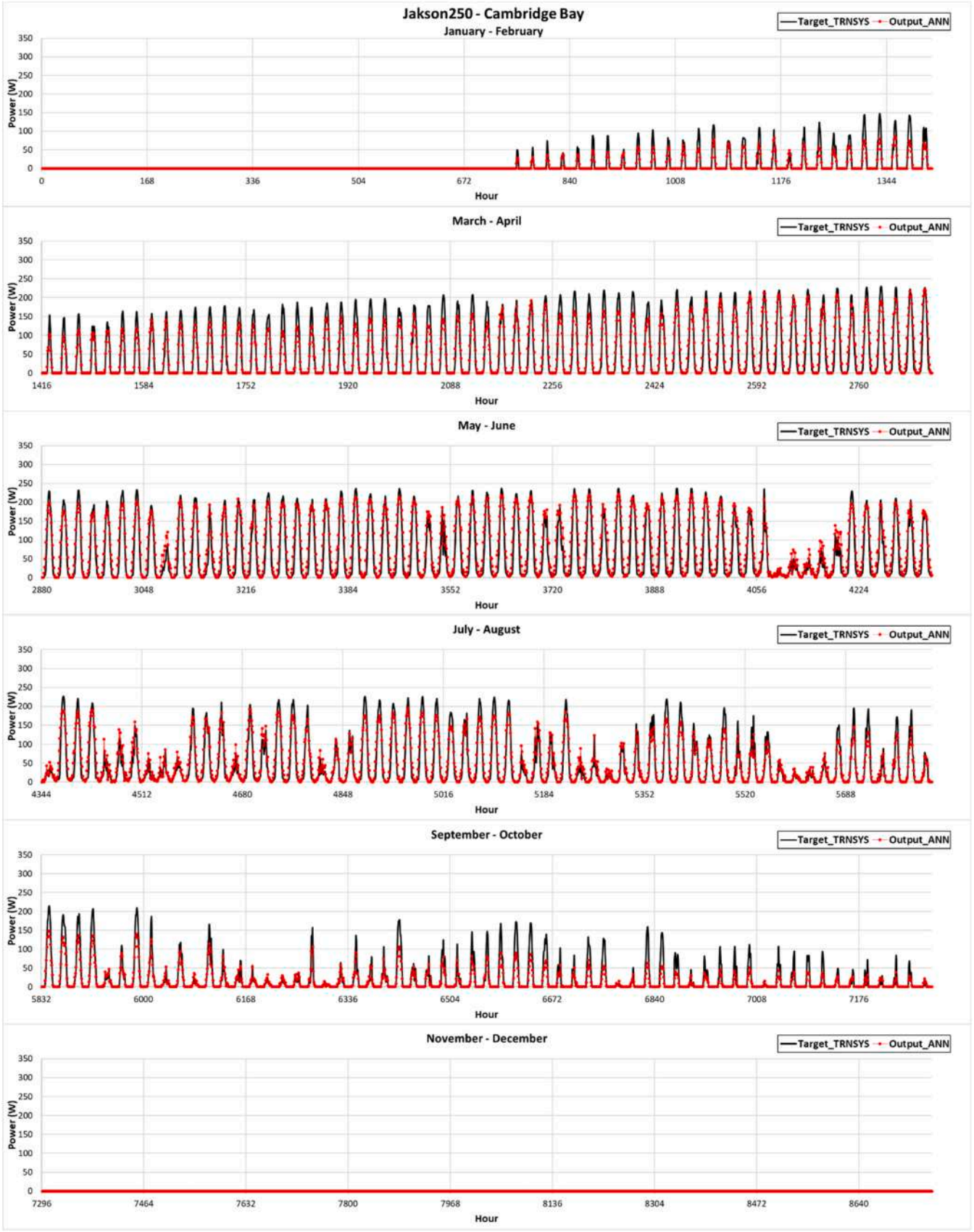

Fig. 13. Hourly trend throughout the year of the electrical energy produced by the Jakson250 PV module in Cambridge Bay calculated with TRNSYS and with the ANN.

Fig. 14. Hourly trend throughout the year of the electrical energy produced by the Panasonic330 PV module in Singapore calculated with TRNSYS and with the ANN.

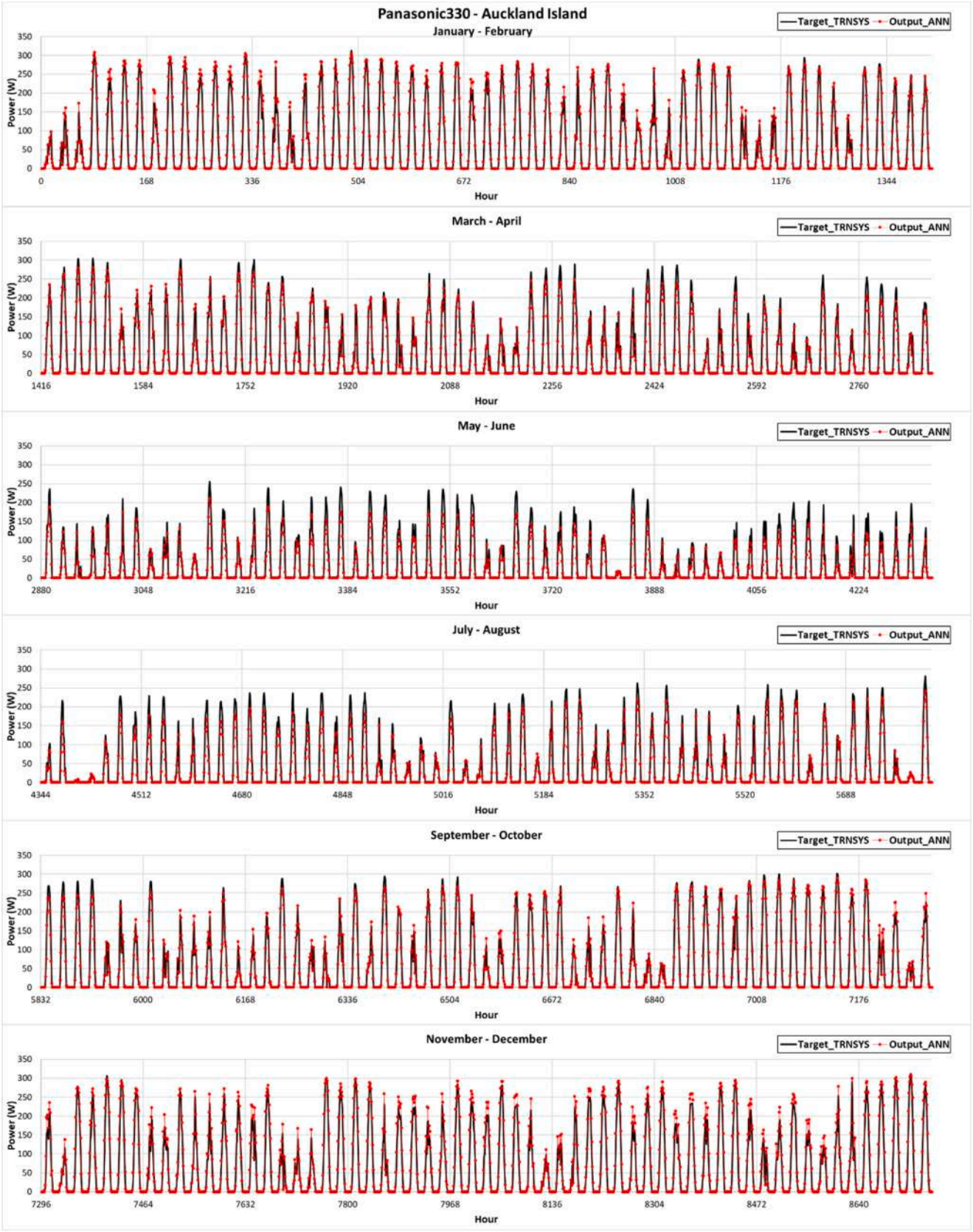

Fig. 15. Hourly trend throughout the year of the electrical energy produced by the Panasonic330 PV module in Auckland Island calculated with TRNSYS and with the ANN.

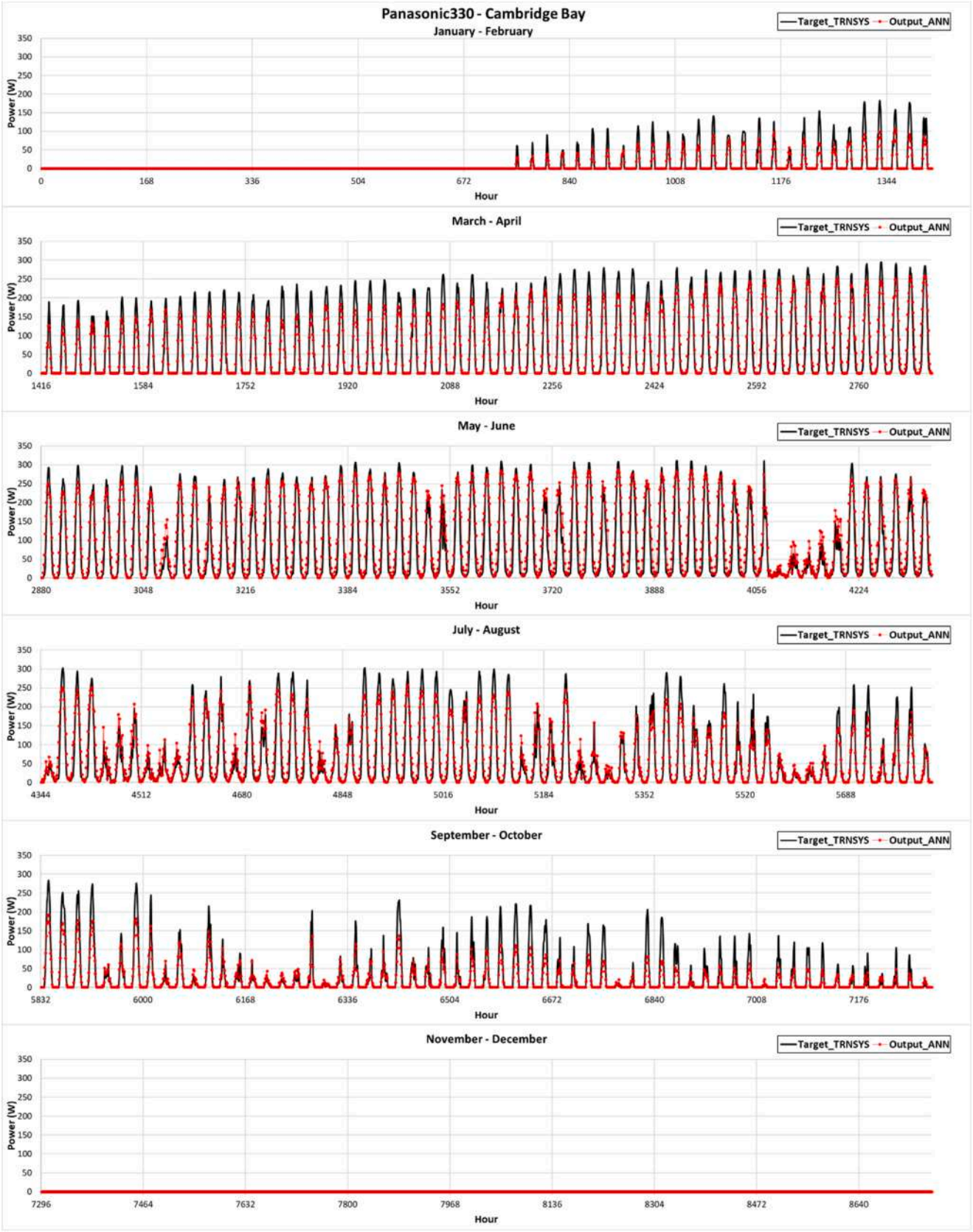

Fig. 16. Hourly trend throughout the year of the electrical energy produced by the Panasonic330 PV module in Cambridge Bay calculated with TRNSYS and with the ANN.

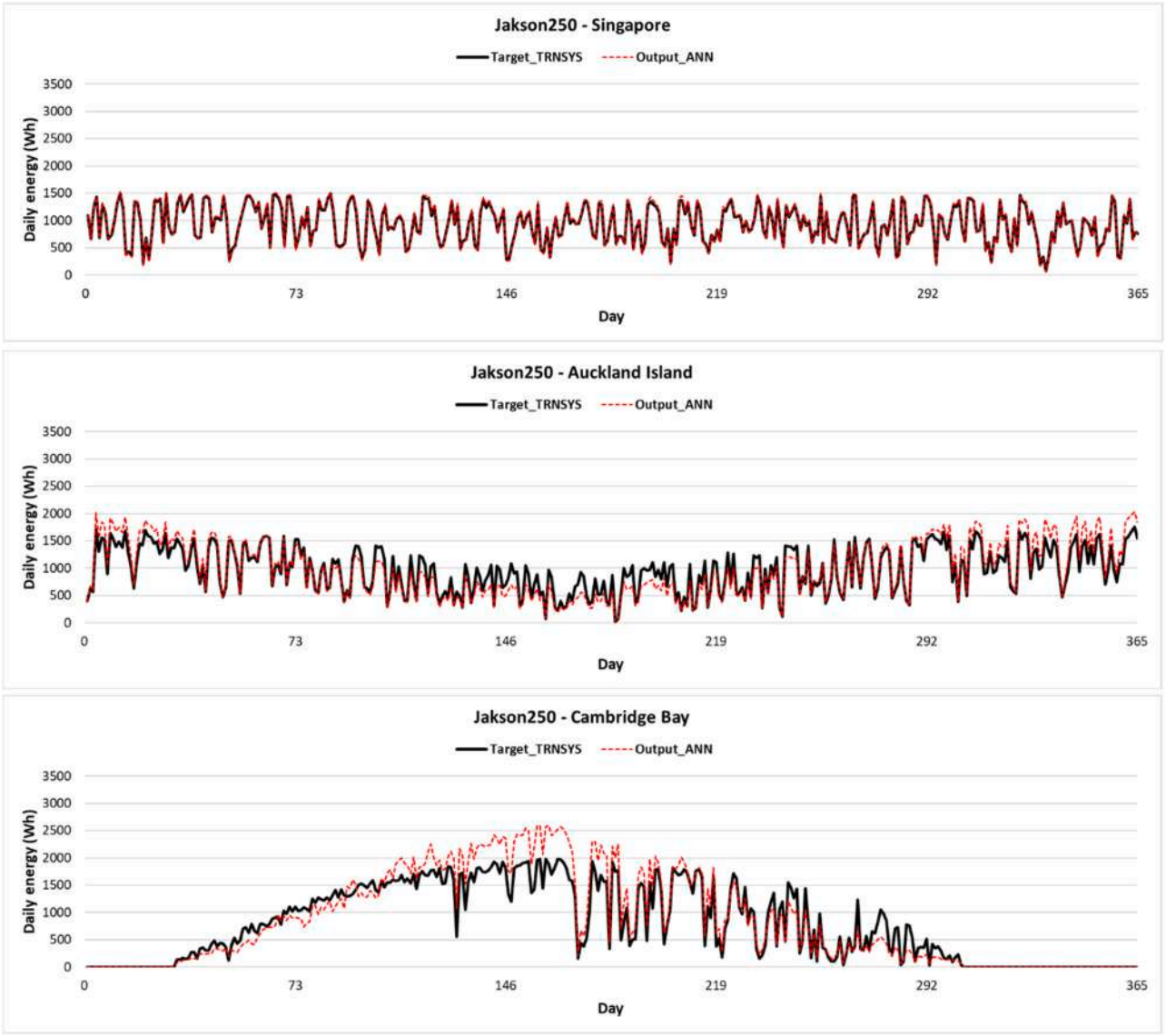

Fig. 17. Daily trend throughout the year of the electrical energy produced by the Jakson250 PV module in Singapore, Auckland and Cambridge Bay calculated with TRNSYS and with the ANN.

3.3. Input and output data for ANN training

The dimensionless input and output data are represented by: the hourly ratio t_{ea} of the external air temperature T_{ea} and the reference temperature $T_{ea,ref}$ of 25° C; the hourly ratio g_h of the total horizontal solar radiation G_h and the reference radiation $G_{h,ref}$ of 1000 W/m^2; the hourly ratio p_{el} of the electrical power P_{el} and the nominal power of the PV module considered, obtained from the product between voltage and current at the point of maximum power P_{mp}. The dataset, comprising pairs of ratios of the air temperature and horizontal total solar radiation data, was randomly divided into three subsets: 70% for training, 15% for testing, and the remaining 15% for validation. Subsequently, both input and output vectors are scaled to fit within the range of [-1, +1] directly within the Matlab software, ensuring equal significance for each input during ANN training. This normalization procedure sets the minimum and maximum values to −1 and 1, respectively. Following the ANN training, the output vector is restored to its original scale through denormalization.

4. Results

4.1. Training of the artificial neural networks

The ANN was trained by varying the number of neurons in the hidden layer; the results, in terms of hourly electrical powers calculated by the ANN and the error vector given by the difference between the training hourly electrical powers and those predicted by the ANN, were saved.

The ANN training process is interrupted when the validation error has increased six times in a row. As shown in Fig. 6a for the case of the ANN of the Jakson PV module with seven neurons, this occurred after four minutes and 194 iterations. The histogram of errors divided into training, validation and testing data is reported in Fig. 6b.

In particular, the training process is interrupted with a gradient value of 8.081×10^{-5} and a damping parameter "μ" value of 1×10^{-7}. In correspondence with epoch 40, there is an increase in the validation error for five consecutive times and in correspondence with epoch 100, there is an increase in the error for three consecutive times. The ANN training is interrupted in correspondence with epoch 194 because since epoch 188 there is an increase in the validation error for the following

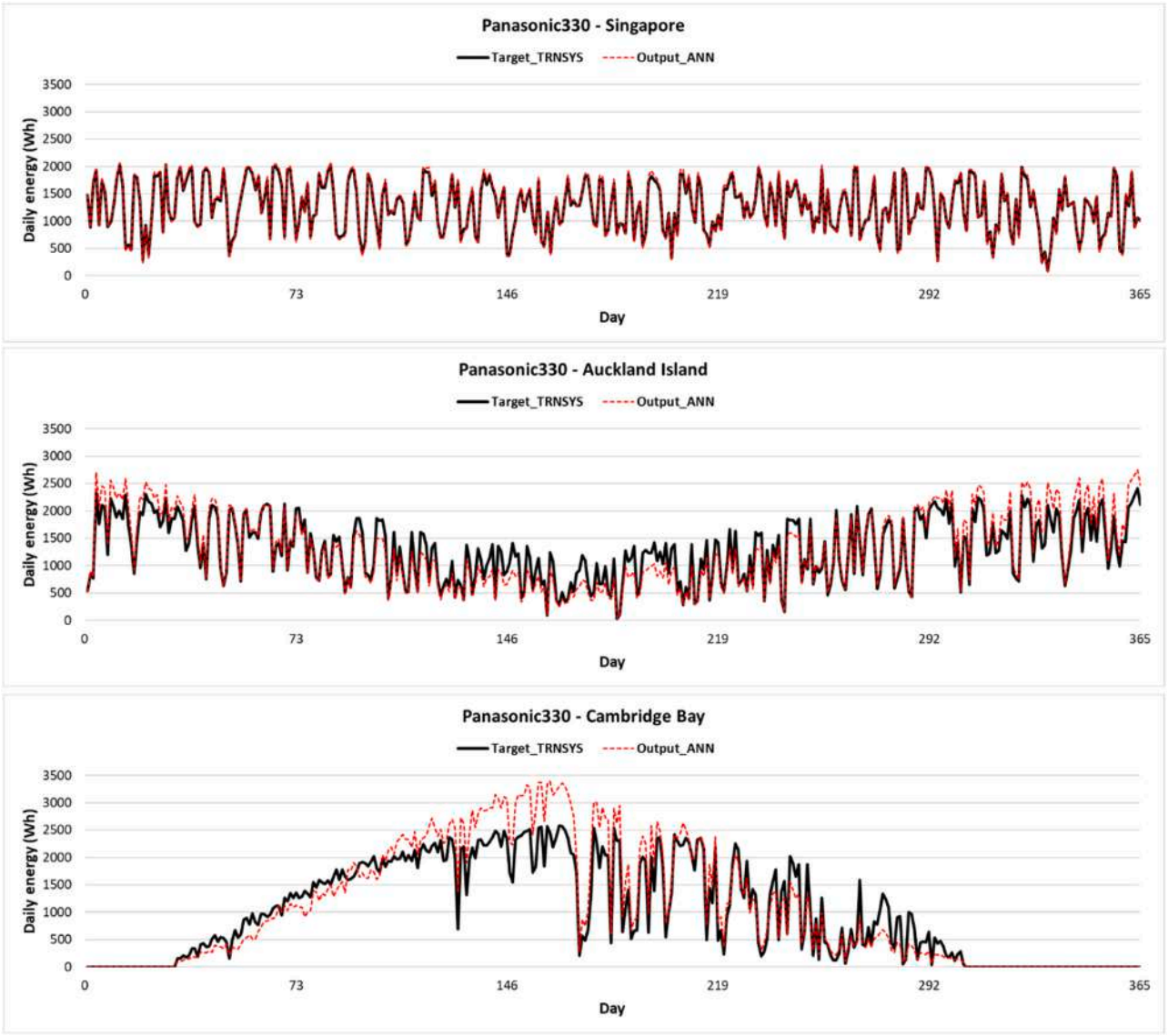

Fig. 18. Daily trend throughout the year of the electrical energy produced by the Panasonic330 PV module in Singapore, Auckland and Cambridge Bay calculated with TRNSYS and with the ANN.

six iterations. The error histogram highlights that most of the training, validation and test data are included in the bins around the zero error. Fig. 7 illustrates the regression diagram for the training, validation, testing and overall processes.

The dashed line represents the perfect result in which the output obtained with the ANN coincides with the target, while the continuous line provides an indication of the relationship between the ANN output obtained and the target. The regression performance is very high given the high value of the R accuracy metric for all data typologies.

The ANN Matlab script and the results obtained, i.e. the dimensionless hourly electrical powers obtained during the ANN training phase and the errors made by the difference between the targets and the ANN outputs, were saved for all PV modules and number of neurons.

From the comparison of the hourly electrical powers calculated with the ANN and with the 5-parameter model, the values of the Root Mean Square Error (RMSE), R-Square (R^2) and Mean Absolute Error (MAE) were obtained [42]. The values obtained by varying the number of neurons in the hidden layer, for all PV modules considered in the training phase, are reported in Table 4.

For all PV modules, the optimal number of neurons was identified by analysing the percentage increase of the RMSE, R^2 and MAE values. For example, for the Jakson module, the metrics are almost unchangeable from the seventh neuron onwards; in this way, the highest value of R^2 and the lowest value of RMSE and MAE are obtained with 7 neurons in the hidden layer. A sharp change in accuracy metrics is observed from one neuron to three neurons in the hidden layer; after the optimal number of neurons, the values remain almost constant, as highlighted by the percentage increase. In the same way, the ANNs related to the other PV modules.

Fig. 8 shows the regression diagrams obtained for the optimal ANNs for each PV module.

The optimization of the accuracy of the ANNs led to regression curves very close to the bisector with very high R^2 and low intercepts and almost unitary angular coefficients for all PV modules.

Moreover, to evaluate the ANN performance as the neurons vary, the errors given by the difference between the target and ANN output values of the dimensionless electrical power were calculated and elaborated in terms of a boxplot in Fig. 9 for all PV modules. In the boxplots, also the nocturnal values were considered despite the differences between the target nil values and those predicted by the ANNs are very low. In

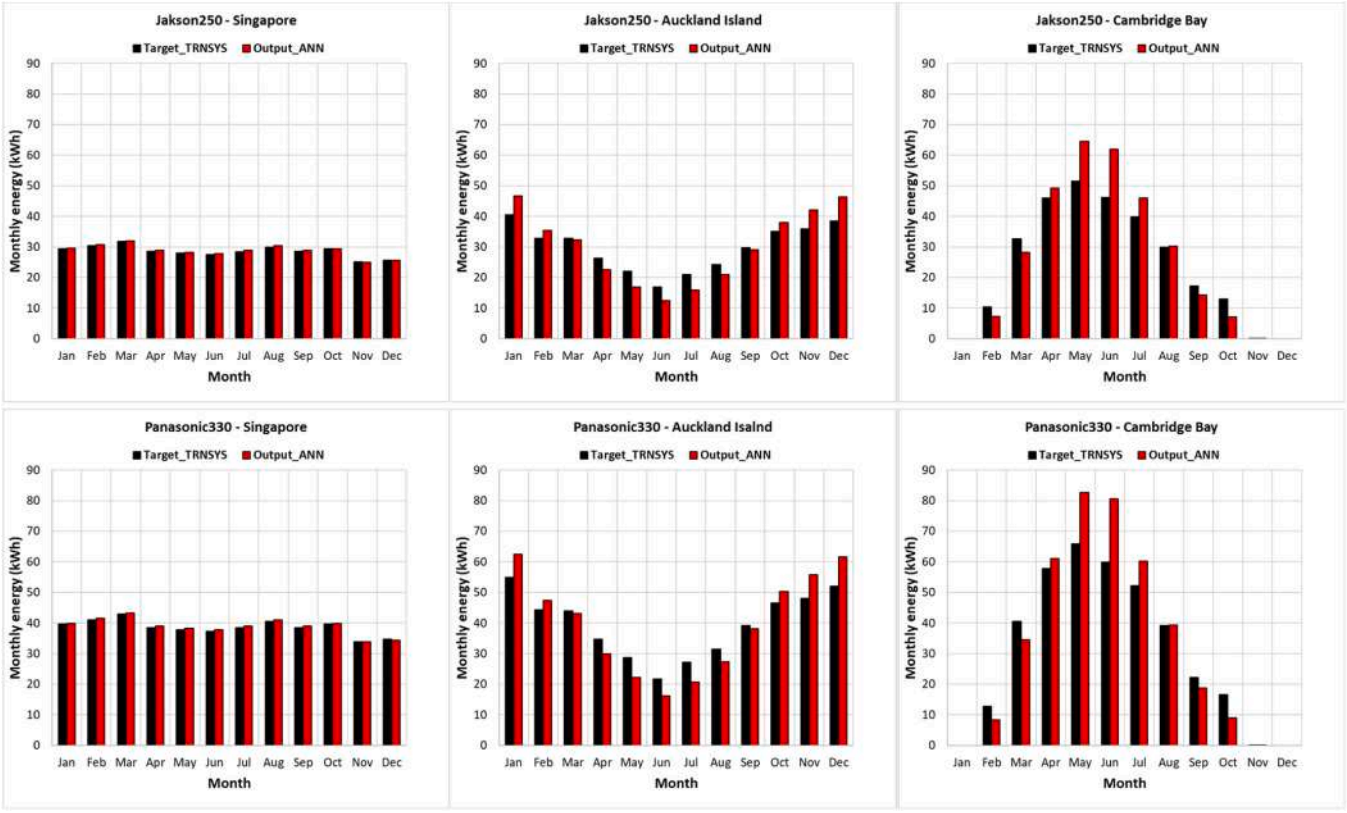

Fig. 19. Monthly electrical energy produced by the Panasonic330 PV module in Singapore, Auckland and Cambridge Bay, calculated with TRNSYS and with the ANN.

addition, the boxplot outliers were not reported to better highlight the mean, variance and symmetry properties of the boxplots.

For all PV modules, a further increase of the neurons compared to the optimal values does not produce noticeable improvements. As expected, the maximum accuracy improvements are obtained by increasing neurons from 1 to 3.

4.2. Validation of the artificial neural networks. Fig. 10 highlights the error dispersion through boxplots for each PV module in all 24 localities of the validation set. Also in this case, the outliers were not shown and the errors during the nocturnal hours were included.

From the Fig. 10, it is evident that the errors are generally low for all PV modules and localities since the boxplot is placed around the nil error. In some localities, the errors are prevalently placed on the positive values which means an underestimation of the dimensionless power, while the ANNs lead to an overestimation in other localities. Overall, the predictions in localities belonging to the Koppen D subgroups, in blue color, highlight a wider error interquartile range, that measures the variance breadth or dispersion around the mean value. This is owing to the very extreme weather conditions characterizing these localities. Nevertheless, the error range can be retained as acceptable.

The next analysis aims to evaluate the accuracy of the ANNs in the prediction of the hourly, daily, monthly and yearly energy produced by the PV modules in the 24 localities considered in the validation phase. This analysis permits the identification of how accuracy metric values are linked to the energy forecasting capacity of the ANNs and the accuracy grade required to obtain low errors in PV energy forecasting.

4.2.1. Hourly analysis. At an hourly level, the localities with the highest, intermediate and lowest accuracy, respectively Singapore, Auckland Island and Cambridge Bay, were selected to evaluate the accuracy of the ANNs. Despite Auckland representing the intermediate locality, since has an accuracy very close to the overall mean accuracy of all localities, most of the localities have values of accuracy metrics between those related to Singapore and Auckland Island. This is owing to the low accuracy, compared to that of the other localities, of some localities belonging the Group D.

The three localities are characterized by extreme geographical placement since Singapore is very close to the equator, Cambridge Bay is placed on a very high positive latitude and Auckland Island is on a very high negative latitude. The produced electrical energy by two characteristic PV modules, the one with the maximum nominal power (Panasonic330) and the one with the minimum nominal power (Jakson250) among all PV modules considered in the network, was considered.

Figs. 11–13 show the hourly trend throughout the year of the electrical energy produced by the Jakson250 PV module in Singapore, Auckland Island and Cambridge Bay calculated with TRNSYS and with the ANN. Instead, the same comparisons are illustrated for the Panasonic330 PV module in Figs. 14–16.

From the figures, the following conclusions can be deducted for both PV modules:

- In Singapore, the highest accuracy demonstrated by the metrics leads to an hourly trend of the electrical power obtained with the ANNs superimposed on that calculated with the 5-parameter of TRNSYS.
- In Auckland Island, the intermediate accuracy demonstrated by the metrics leads to an hourly trend of the electrical power obtained with the ANNs almost superimposed on that calculated with the 5-parameter of TRNSYS; a slight underestimation during the peak hours can be observed in the autumnal and winter period of the southern hemisphere (from March to September) and, vice versa, a slight overestimation in the spring and summer period (from November to February) of the southern hemisphere.
- In Cambridge Bay, the worst accuracy demonstrated by the metrics leads to an underestimated hourly electrical power calculated with the ANNs compared to the TRNSYS one during the peak hours: this

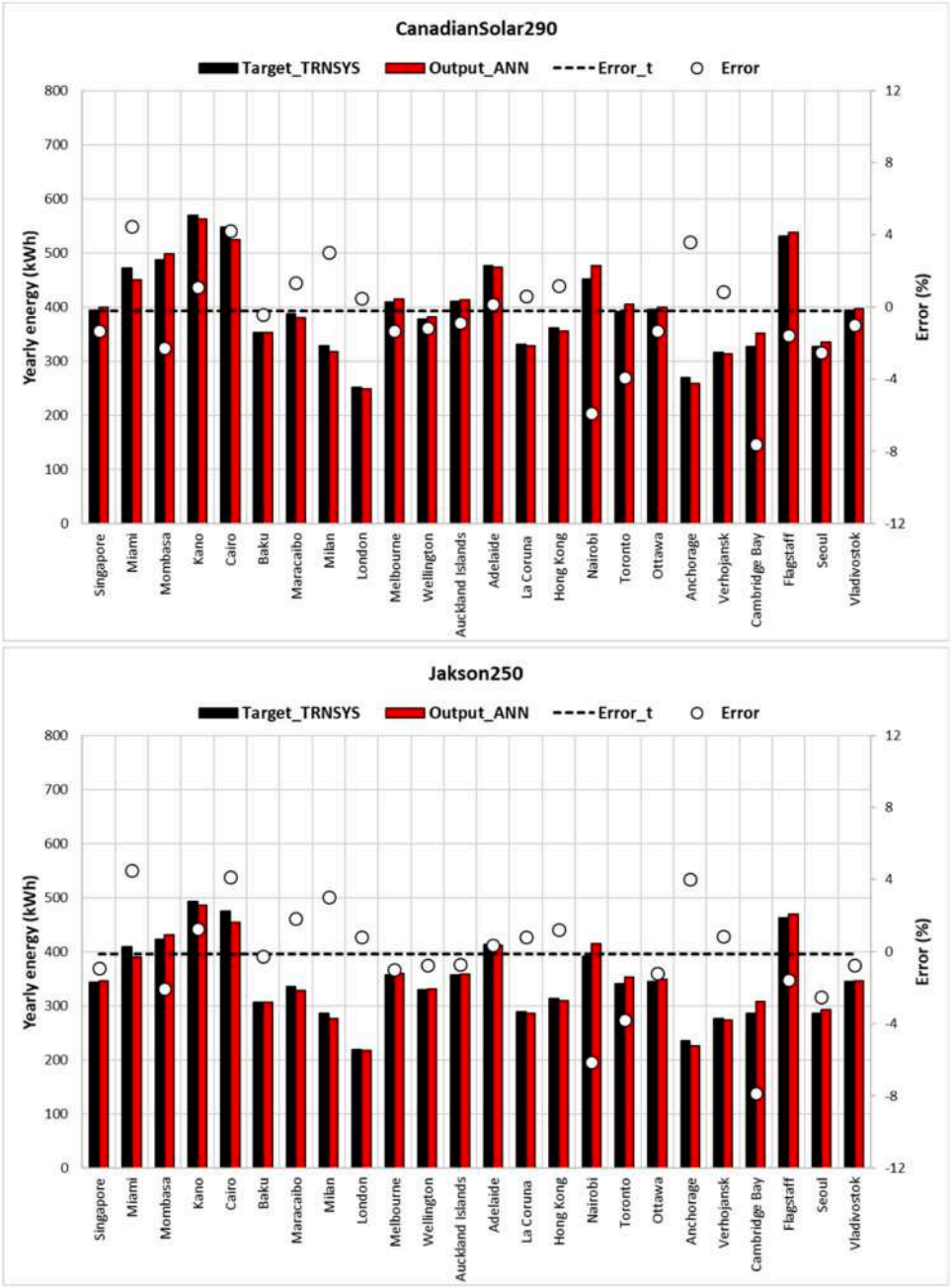

Fig. 20. Yearly electrical energy produced by the CanadianSolar290 and Jakson250 PV modules in the 24 localities of the validation set calculated with TRNSYS and with the ANN.

underestimation is quite slight in the spring and summer period of the northern hemisphere (from March to August) and, increases during the autumnal and winter period of the northern hemisphere (from September to February, except from November to January, when the locality has no daylight hours); in May and June, an overestimation is observed during the nocturnal hours, when there are 24 hours of daylight.

- The qualitative trends obtained from the ANNs follow perfectly the TRNSYS trend, also when abrupt variations occur.
- The accuracy improves in the spring, summer, and autumn periods both in the northern and southern hemispheres, namely when the production of electrical energy is the highest.

Considering that the ANNs can reliably predict the change in the hourly energy produced in the locality characterized by very extreme weather conditions and by worst accuracy in terms of accuracy metrics, the previous considerations demonstrate that the ANNs are very reliable in the forecasting of the hourly electrical energy produced by any PV module belonging to the network. This reliability becomes very high in the majority of the worldwide localities since they are characterized by intermediate weather conditions compared to those of Cambridge Bay and Singapore. Most of the worldwide localities belong to the Koppen groups A, B and C, where the ANNs demonstrated the highest reliability and accuracy.

4.2.2. Daily analysis. Similarly to the hourly analysis, at a daily level, the same PV modules and localities were considered to evaluate the performance of the ANNs. Figs. 17 and 18 illustrate the trend of the daily electrical energy produced, respectively, by the Jakson250 and Panasonic330 PV modules in the three characteristic localities.

The figures provide further details on the accuracy and reliability of

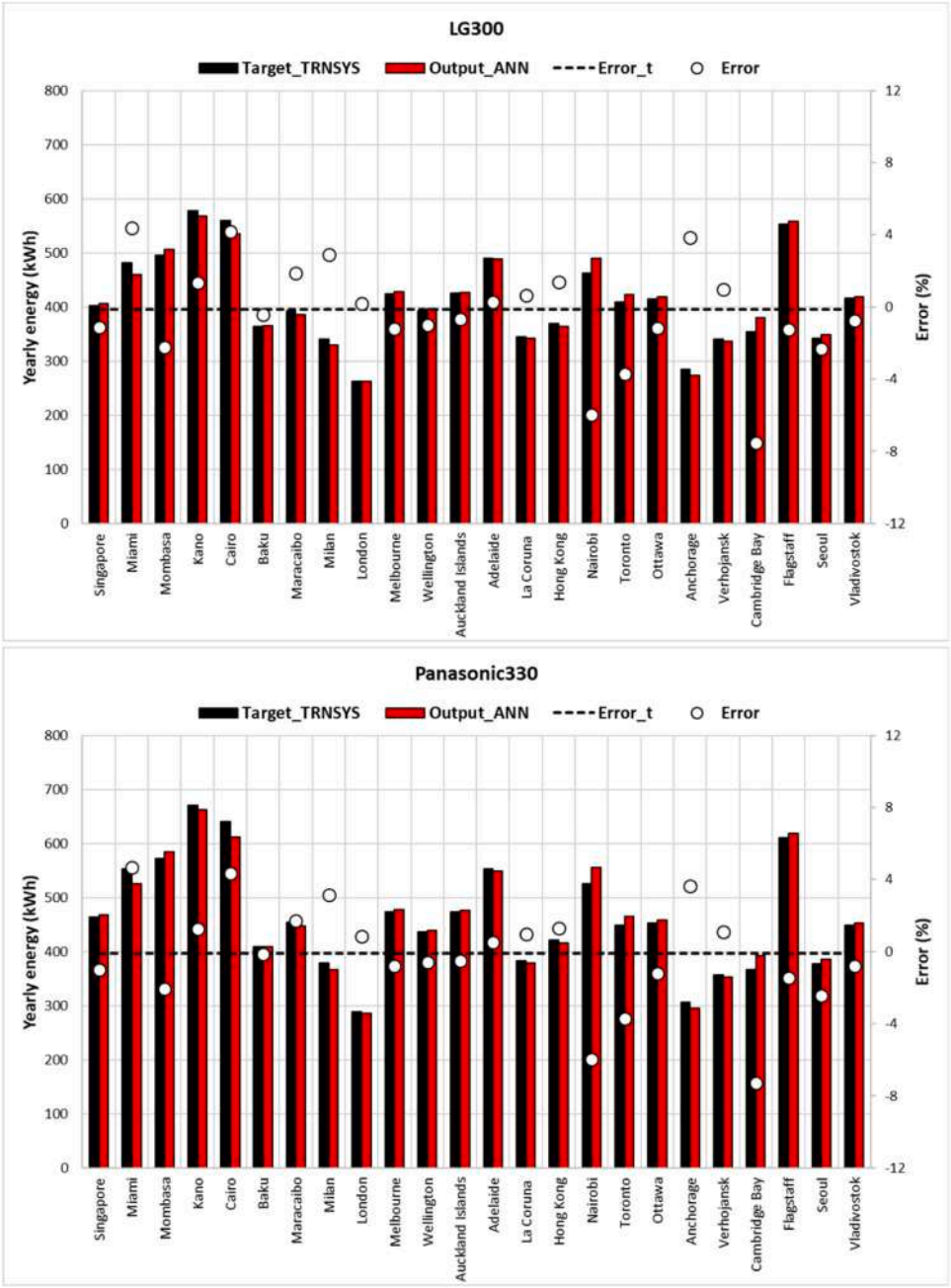

Fig. 21. Yearly electrical energy produced by the LG300 and Panasonic330 PV modules in the 24 localities of the validation set calculated with TRNSYS and with the ANN.

the ANNs in the different localities by changing the season:

- In Singapore, the daily energy forecast is excellent in all seasons.
- In Auckland Island, the highest accuracy is observed in the intermediate seasons, while in the summer and winter period, an overall overestimation and underestimation, respectively, is observed on the daily trends.
- In Cambridge Bay, the daily energy exhibits great accuracy during the winter season and the first part of the spring season, and an evident overestimation in the days characterized by 24 hours of daylight, namely the second part of the spring season and in the first part of the summer period, given to the greater estimations during the nocturnal hours that are prevalent compared to the underestimation of the energy during the peak hours; instead, this overestimation can be considered low during the second part of the summer season; finally, the autumnal season is characterized by very high accuracy in the first part, while in the second part, the ANNs underestimate the daily energy.
- In general, also in this case, the qualitative trends can be considered very close to those deriving from the 5-parameter model.
- This analysis confirms that the ANNs are very reliable in daily energy forecasting, given that the majority of worldwide localities considered have accuracy metrics between those obtained for Singapore and Auckland Island.

4.2.3. Monthly analysis. At a monthly level, the comparison between the results obtained from the ANNs compared with those obtained from TRNSYS is shown in Fig. 19 for the three characteristic localities and the Jakson250 and Panasonic330 PV modules.

The comparison highlights also the high accuracy of the ANNs in the worldwide monthly energy forecasting and the main findings observed

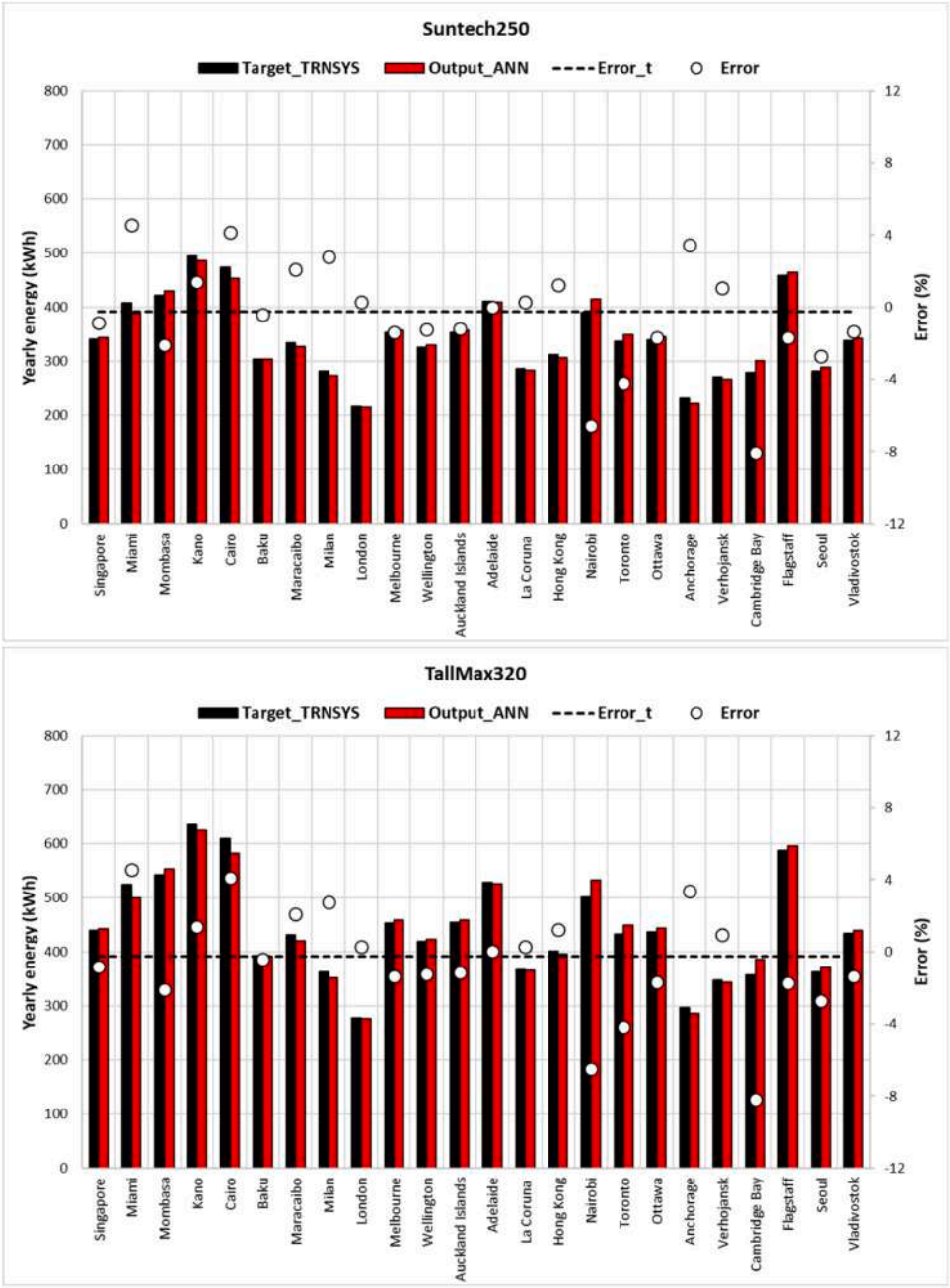

Fig. 22. Yearly electrical energy produced by the Suntech250 and TallMax320 PV modules, in the 24 localities of the validation set, calculated with TRNSYS and with the ANN.

in the hourly and daily analyses. In addition, this further analysis points out that the highest monthly error occurs in the summer months of worldwide localities with very high positive or negative latitudes when the day duration is much higher than the night duration; in particular, in Cambridge Bay, this phenomenon is amplified given the presence of 24 hours of daylight in May, June and July.

4.2.4. Yearly analysis. The yearly analysis is fundamental to summarize the previous findings and to evaluate the relation between the accuracy metrics obtained and the reliability and accuracy of the ANNs in the worldwide yearly energy forecasting.

The goodness of the ANNs created was also estimated by comparing the predicted yearly electrical energy produced in each locality of the validation set with the yearly energy obtained with the target hourly electrical power provided by the TRNSYS software. Figs. 20–22 show the yearly energies, for all six PV modules by varying the locality, obtained with the ANN and TRNSYS software and the percentage relative errors.

The different ANNs related to the various PV modules are perfectly able to predict the energy in all localities considered since the relative errors are very small. Consequently, in the locality where the ANNs highlighted the worst accuracy with the lowest R^2 and highest RMSE and MAE, the maximum error in the yearly energy forecasting is 8%, which is very low considering that any complex non-linear model was used to solve the exponential equation system characterizing a PV 5-parameter model. It can be deduced that the slight hourly, daily, and monthly overestimation or underestimation highlighted are compensated at a yearly level.

ANNs have undergone global validation and are applicable for predicting the electrical energy output of a PV module without reliance on the TRNSYS software.

Table 5
Elements of the weight matrices w_1 and w_2 and bias matrices b_1 and b_2 for each PV module of the ANNs.

Weight matrix w_1	
CanadianSolar290	$w_1 = \begin{bmatrix} 6.39 & -4.93 & 6.72 & -0.59 & -3.02 & 2.64 & -1.02 \\ -4.05 & -0.27 & -2.26 & 1.35 & -5.57 & 1.12 & -4.02 \end{bmatrix}$
Jakson250	$w_1 = \begin{bmatrix} 0.05 & 0.39 & -2.96 & -6.51 & -3.92 & -6.47 & 2.70 \\ 1.09 & 1.52 & 2.88 & 0.12 & 1.54 & 0.04 & 5.44 \end{bmatrix}$
LG300	$w_1 = \begin{bmatrix} -5.24 & 1.72 & 0.77 & -2.56 & 3.43 & -4.56 & -0.76 \\ -0.44 & -1.90 & 1.09 & -3.74 & -1.28 & -0.54 & 4.16 \end{bmatrix}$
Panasonic330	$w_1 = \begin{bmatrix} 2.87 & 8.83 & -0.88 & 7.94 & 0.75 & -6.62 & -0.93 - 0.64 \\ 2.53 & -0.90 & -2.07 & 0.82 & 1.84 & 3.13 & 1.70 - 3.93 \end{bmatrix}$
Suntech250	$w_1 = \begin{bmatrix} 0.09 & -1.31 & 6.91 & 0.31 & 6.70 & -1.99 \\ 1.65 & 1.97 & 0.11 & 2.75 & 0.47 & -7.42 \end{bmatrix}$
TallMax320	$w_1 = \begin{bmatrix} 0.08 & -1.33 & 6.91 & 0.37 & 6.70 & -1.99 \\ 1.62 & 1.98 & 0.11 & 2.58 & 0.45 & -7.46 \end{bmatrix}$
Weight matrix w_2	
CanadianSolar290	$w_2 = [0.06 \quad 0.15 \quad -0.11 \quad 1.02 \quad -0.37 \quad 0.26 \quad -0.10]$
Jakson250	$w_2 = [2.07 \quad -0.94 \quad 0.15 \quad 1.76 \quad 0.27 \quad -1.78 \quad 0.43]$
LG300	$w_2 = [-0.57 \quad -0.46 \quad 0.78 \quad -0.76 \quad -0.46 \quad 0.74 \quad 0.12]$
Panasonic330	$w_2 = [0.05 \quad -0.09 \quad 4.22 \quad 0.11 \quad 5.27 \quad 0.04 \quad 0.630.12]$
Suntech250	$w_2 = [0.47 \quad 0.47 \quad -0.36 \quad 0.21 \quad 0.37 \quad -0.30]$
TallMax320	$w_2 = [0.48 \quad 0.45 \quad -0.37 \quad 0.22 \quad 0.39 \quad -0.29]$
Bias vector b_1	
CanadianSolar290	$b_1 = \begin{bmatrix} -6.11 \\ 1.45 \\ 1.24 \\ 0.74 \\ -7.23 \\ 0.18 \\ 3.37 \end{bmatrix}$
Jakson250	$b_1 = \begin{bmatrix} 0.08 \\ -0.22 \\ 2.05 \\ 1.21 \\ -0.99 \\ 0.12 \\ 7.02 \end{bmatrix}$
LG300	$b_1 = \begin{bmatrix} 2.54 \\ -1.21 \\ 0.39 \\ -5.50 \\ 1.18 \\ 2.08 \\ -2.47 \end{bmatrix}$
Panasonic330	$b_1 = \begin{bmatrix} -2.89 \\ -2.42 \\ -2.08 \\ -0.56 \\ 1.95 \\ -0.83 \\ 0.78 \\ 3.34 \end{bmatrix}$
Suntech250	$b_1 = \begin{bmatrix} 1.03 \\ 0.89 \\ -1.37 \\ -2.30 \\ -0.96 \\ -8.76 \end{bmatrix}$
TallMax320	$b_1 = \begin{bmatrix} 1.02 \\ 0.91 \\ -1.37 \\ -2.24 \\ -0.97 \\ -8.79 \end{bmatrix}$
Bias vector b_2	
CanadianSolar290	$b_2 = [-0.48]$
Jakson250	$b_2 = [-0.32]$
LG300	$b_2 = [-0.56]$
Panasonic330	$b_2 = [-0.86]$
Suntech250	$b_2 = [-0.42]$
TallMax320	$b_2 = [-0.41]$

Table 6
Parameters required for the normalization of the inputs and denormalization of the output.

Denormalization	CanadianSolar290 $p_{el,min} = 0$ $p_{el,max} = 1.039$	Jakson250 $p_{el,min} = 0$ $p_{el,max} = 1.032$	LG300 $p_{el,min} = 0$ $p_{el,max} = 1.029$	Panasonic330 $p_{el,min} = 0$ $p_{el,max} = 1.074$	Suntech250 $p_{el,min} = 0$ $p_{el,max} = 1.048$	TallMax320 $p_{el,min} = 0$ $p_{el,max} = 1.011$
Normalization	$t_{ea}(-)$ $x_{min} = -2.440$ $x_{max} = 1.784$			$g_h(-)$ $x_{min} = 0.000$ $x_{max} = 1.236$		

4.3. Model equation for the PV electrical power forecasting based on trained ANNs. Based on the work developed by Das et al. [54], an empirical model equation can be obtained starting from the knowledge of the weight and bias values of the optimal ANNs. The dimensionless hourly electrical power produced can be calculated using Eqs. (34)-(36).

$$p_{el,n} = b_2 + \sum_{i=1}^{n_i} w_{2,1i}\left(\frac{2}{1+e^{-2A_i}} - 1\right) \tag{34}$$

where,

$$A_i = b_{1,i} + w_{1,1i} \bullet t_{ea,n} + w_{1,2i} \bullet g_{h,n} \tag{35}$$

Finally, the output is to be denormalized as follows:

$$p_{el} = \frac{1}{2}(p_{el,n} + 1)(p_{el,max} - p_{el,min}) + p_{el,min} \tag{36}$$

In Table 5, the values of the elements of the weight matrices w_1 and w_2 and bias matrices b_1 and b_2 are reported for each PV module of the ANNs.

Instead, Table 6 lists all the parameters required for the normalization of the inputs and denormalization of the output.

4.4. Relative input-output importance by the Garson method. To extract the physical behavior of the six PV modules located in the 24 localities used for the ANN training, the generalized procedure of the Garson method, described in Section 2.2, was used to evaluate the percentage impact of the dimensionless air temperature and horizontal total solar radiation on the dimensionless PV power produced.

The results of this analysis are summarized in terms of the percentage sensitivity index S_{ij} of the input *i* on the output *j* for each PV module in Fig. 23.

The index demonstrates that the effect produced by the air temperature and solar radiation depends on the PV module typology, namely on its electrical and thermal characteristics. In particular, the electrical behavior of the CanadianSolar290 PV modules depends almost on the same measure of the hourly variation of the two inputs, while that of Suntech250, TallMax320 PV and LG300 PV modules depends slightly more on the air temperature. Instead, the electrical behavior of the

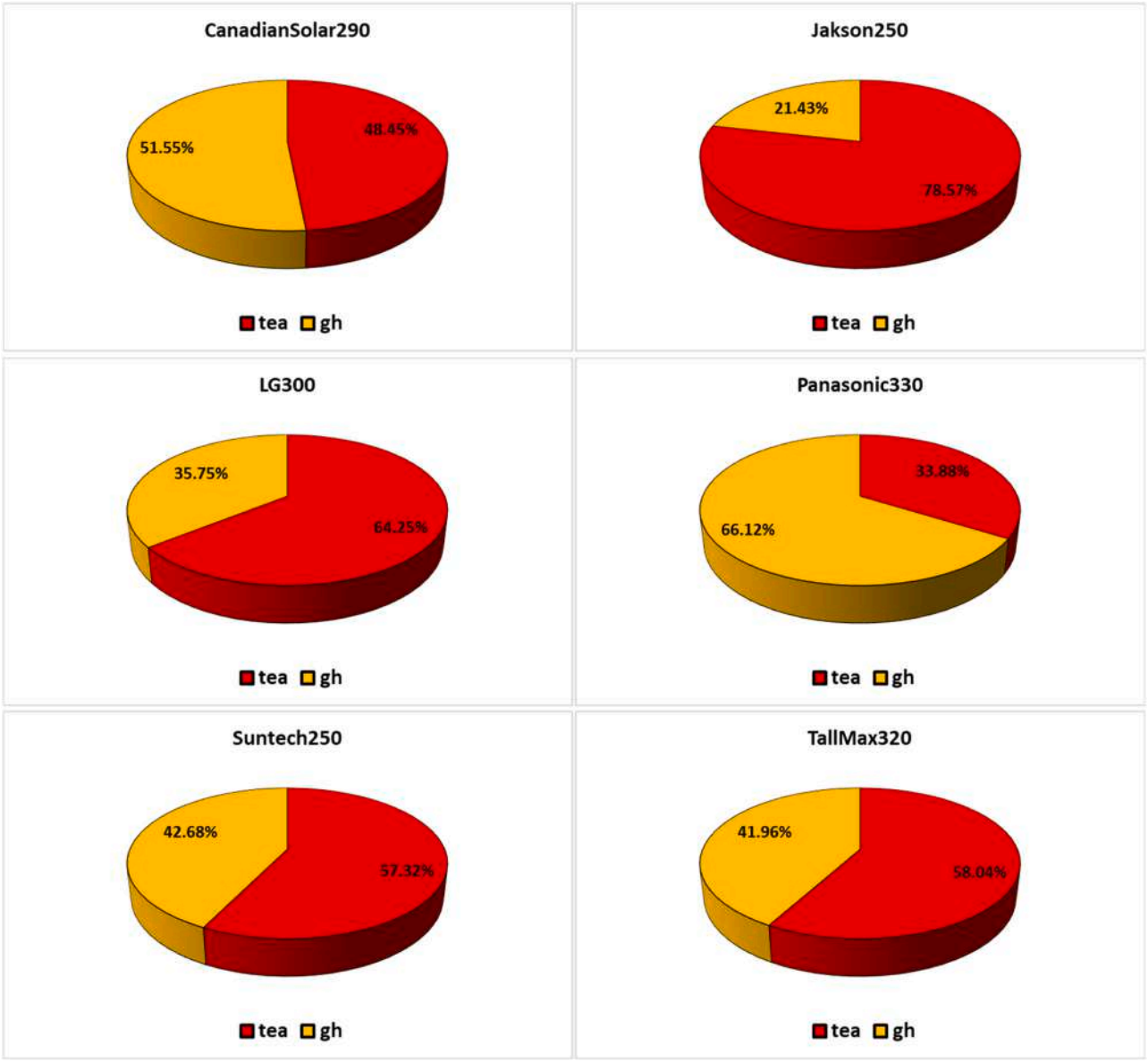

Fig. 23. Percentage sensitivity index of the dimensionless air temperature and horizontal total solar radiation on the dimensionless PV power produced for all PV modules belonging to the ANNs.

Jakson250 PV module depends strongly on the air temperature, while, vice versa that of the Panasonic330 is strongly influenced by solar radiation.

By comparing the thermal and electrical parameters of the six PV modules can be highlighted that:

- The Jakson250 PV module is characterized by the lowest reference efficiency and highest NOCT; for this reason, the thermal losses, and consequently the energy production, of the PV module are greatly influenced by the temperature.
- The Panasonic330 PV module is characterized by the highest reference efficiency, number of cells, open-circuit voltage, voltage at the maximum power point, percentage variation of open-circuit voltage with the temperature and the lowest current at the maximum power point; given the high efficiency, the solar radiation is the main responsible of the energy production.

5. *Conclusions*

This research presents a comprehensive analysis of Artificial Neural Networks (ANNs) for the accurate prediction of electrical power output from PhotoVoltaic (PV) modules across various geographic locations. ANNs were trained, optimized, and validated on a global scale across various types of PV modules, assessing their accuracy and reliability in predicting worldwide hourly, daily, monthly, and yearly energy production.

The study systematically explored the impact of varying the number of neurons in the hidden layer of the ANN on prediction performance. By monitoring error metrics such as RMSE, R^2 and MAE, optimal configurations were identified for different PV modules. Notably, significant improvements in accuracy were observed by increasing neurons from 1 to 3, beyond which marginal gains were achieved.

The validation process across 24 diverse localities further underscored the robustness of the ANN models. Despite extreme weather

conditions in certain regions, the ANNs consistently demonstrated low prediction errors, validating their efficacy across different climates.

In the training phase, ANNs showed a maximum mean absolute error of 3.5%, while in the validation phase, developed considering other localities and PV modules, the hourly relative error is in all cases below 5%.

Hourly, daily, monthly, and yearly analyses provided granular insights into prediction accuracy under varying temporal scales. Overall, hourly power forecasting is less accurate but acceptable in localities around the globe with very extreme weather conditions, such as those characterized by extended daylight or extreme temperature fluctuations. At a monthly level, the highest errors occur in the summer months of worldwide localities with very high positive or negative latitudes when the day duration is much higher than the night duration. On a yearly basis, in the locality where the ANNs highlighted the worst accuracy, the maximum error in the yearly energy forecasting is 8%, which is very low considering that any complex non-linear model was used to solve the exponential equation system characterizing a PV 5-parameter model. It can be deduced that the slight hourly, daily, and monthly overestimation or underestimation highlighted are compensated at a yearly level.

To enhance user-friendly forecasting of PV module performance, empirical equations derived from the trained ANNs, dependent on weight and bias matrices, were provided minimizing the expertize required.

In the final analysis, the Garson method was employed to identify the relative input-output importance, quantifying the percentage impact of weather conditions on power production. In other words, sensitivity analyses revealed the nuanced influence of air temperature and solar radiation on PV power output, highlighting the module-specific dependencies.

The developed hourly ANNs prove instrumental in decision-making and real-time processes, facilitating energy flow management in the grid, offering forecasts for hourly, daily, monthly, and yearly performance, and serving as an alternative to classical methods for PV system sizing. The results obtained using ANN training and validation in many localities around the globe constitute a concrete tool to detect the performance of PV systems around the world. In addition, the results can be used by other researchers as a reference to compare their investigations.

The application of ANNs allows for the rapid and straightforward estimation of electric power produced by a PV module, eliminating the need for computationally expensive algorithm codes.

Several promising avenues can enhance this research work, such as exploring the use of ANN architectures like recurrent or convolutional neural networks, integrating additional environmental data such as cloud cover and humidity, integrating ANNs developed with energy management systems to optimize energy scheduling and enhance grid stability. These future directions hold promise for advancing the field of PV energy forecasting, leading to more resilient and efficient renewable energy integration.

Author statements

All authors have realized and accepted the data of the submitted manuscript. The paper presents unique work not earlier published in a similar form and not presently under consideration by another Journal. The authors followed ethical guidelines.

CRediT authorship contribution statement

Nicoletta Matera: Writing – review & editing, Writing – original draft, Visualization, Validation, Software, Resources, Methodology, Investigation, Formal analysis, Data curation, Conceptualization. **Michela Longo**: Writing – review & editing, Writing – original draft, Visualization, Supervision, Resources, Project administration, Investigation, Funding acquisition, Formal analysis. **Sonia Leva**: Writing – review & editing, Writing – original draft, Visualization, Supervision, Resources, Project administration, Investigation, Funding acquisition, Formal analysis..

Declaration of Competing Interest

I have no relevant interest(s) to disclose.

Data availability

Data will be made available on request.

Acknowledgments

This study was partly carried out within the MOST – Sustainable Mobility Center and received funding from the European Union Next-GenerationEU (PIANO NAZIONALE DI RIPRESA E RESILIENZA (PNRR) – MISSIONE 4 COMPONENTE 2, INVESTIMENTO 1.4 – D.D. 1033 17/06/2022, CN00000023) and was partly carried out in MESSI – Management Energy Systems for Smart Islands project, within the PRIN PROGETTI DI RICERCA DI RILEVANTE INTERESSE NAZIONALE – Bando 2022 and received funding from the European Union Next-GenerationEU (PIANO NAZIONALE DI RIPRESA E RESILIENZA - PNRR MISSIONE 4 COMPONENTE 2, INVESTIMENTO 1.1 –D.D. n. 104 del 02/02/2022, 2022HMYX2C). This manuscript reflects only the authors' views and opinions, neither the European Union nor the European Commission can be considered responsible for them.

References

[1] F. Spertino, A. Ciocia, A. Mazza, M. Nobile, A. Russo, G. Chicco, Voltage control in low voltage grids with independent operation of on-load tap changer and distributed photovoltaic inverters, ISSN 0378-7796, Electric Power Syst. Res. 211 (2022) 108187, https://doi.org/10.1016/j.epsr.2022.108187.

[2] S. Saadatmandi, G. Chicco, F. Giordano and M. Arnone, Reducing the curtailment of photovoltaic energy production through smart electric vehicle charging, 2022 AEIT International Annual Conference (AEIT), Rome, Italy, 2022, Pages 1-6, https://doi.org/10.23919/AEIT56783.2022.9951712.

[3] V.J. Chin, Z. Salam, K. Ishaque, Cell modelling and model parameters estimation techniques for photovoltaic simulator application: A review, ISSN 0306-2619, Appl. Energy 154 (2015) 500–519, https://doi.org/10.1016/j.apenergy.2015.05.035.

[4] R. Rajesh, M.C. Mabel, A comprehensive review of photovoltaic systems, ISSN 1364-0321, Renew. Sustain. Energy Rev. 51 (2015) 231–248, https://doi.org/10.1016/j.rser.2015.06.006.

[5] D. Mazzeo, M.S. Herdem, N. Matera, M. Bonini, J.Z. Wen, J. Nathwani, G. Oliveti, Artificial intelligence application for the performance prediction of a clean energy community, ISSN 0360-5442, Energy 232 (2021) 120999, https://doi.org/10.1016/j.energy.2021.120999.

[6] S.M. Miraftabzadeh, M. Longo, F. Foiadelli, M. Pasetti, R. Igual, Advances in the application of machine learning techniques for power system analytics: a survey, ISSN 1996-1073, Energies 14 (2021) 4776, https://doi.org/10.3390/en14164776.

[7] D. Mazzeo, N. Matera, G. Peri, G. Scaccianoce, Forecasting green roofs' potential in improving building thermal performance and mitigating urban heat island in the Mediterranean area: an artificial intelligence-based approach, ISSN 1359-4311, Appl. Ther. Eng. 222 (2023) 119879, https://doi.org/10.1016/j.applthermaleng.2022.119879.

[8] A. Dolara, F. Grimaccia, S. Leva, M. Mussetta, E. Ogliari, A physical hybrid artificial neural network for short term forecasting of PV plant power output, ISSN 1996-1073, Energies 8 (2) (2015) 1138–1153, https://doi.org/10.3390/en8021138.

[9] D. Mazzeo, S. Leva, N. Matera, K.J. Kontoleon, S. Saboor, B. Pirouz, M. R. Elkadeem, A user-friendly and accurate machine learning tool for the evaluation of the worldwide yearly photovoltaic electricity production, ISSN 2352-4847, Energy Rep. 9 (2023) 6267–6294, https://doi.org/10.1016/j.egyr.2023.05.221.

[10] A. Mellit, A.M. Pavan, E. Ogliari, S. Leva, V. Lughi, Advanced methods for photovoltaic output power forecasting: a review, Appl. Sci. 10 (2) (2020) 487, https://doi.org/10.3390/app10020487.

[11] N. Matera, D. Mazzeo, C. Baglivo, P.M. Congedo, Hourly forecasting of the photovoltaic electricity at any latitude using a network of artificial neural networks, ISSN 2213-1388, Sustain. Energy Technol. Assess. 57 (2023) 103197, https://doi.org/10.1016/j.seta.2023.103197.

[12] O.T. Huxley, J. Taylor, A. Everard, J. Briggs, K. Tilley, J. Harwood, A. Buckley, The uncertainties involved in measuring national solar photovoltaic electricity generation, ISSN 1364-0321, Renew. Sustain. Energy Rev. 156 (2022) 112000, https://doi.org/10.1016/j.rser.2021.112000.

[13] N. Zhao, F. You, Sustainable power systems operations under renewable energy induced disjunctive uncertainties via machine learning-based robust optimization,

ISSN 1364-0321, Renew. Sustain. Energy Rev. 161 (2022) 112428, https://doi.org/10.1016/j.rser.2022.112428.
[14] B. Li, C. Delpha, D. Diallo, A. Migan-Dubois, Application of artificial neural networks to photovoltaic fault detection and diagnosis: a review, ISSN 1364-0321, Renew. Sustain. Energy Rev. 138 (2021) 110512, https://doi.org/10.1016/j.rser.2020.110512.
[15] H. Yang, X. Liu, D. Zhang, T. Chen, C. Li, W. Huang, Machine learning for power system protection and control, ISSN 1040-6190, Electr. J. 34 (Issue 1) (2021) 106881, https://doi.org/10.1016/j.tej.2020.106881.
[16] L. Yin, Q. Gao, L. Zhao, B. Zhang, T. Wang, S. Li, H. Liu, A review of machine learning for new generation smart dispatch in power systems, ISSN 0952-1976, Eng. Appl. Artif. Intell. 88 (2020) 103372, https://doi.org/10.1016/j.engappai.2019.103372.
[17] U.K. Das, K.S. Tey, M. Seyedmahmoudian, S. Mekhilef, M.Y.I. Idris, W. Van Deventer, B. Horan, A. Stojcevski, Forecasting of photovoltaic power generation and model optimization: a review, ISSN 1364-0321, Renew. Sustain. Energy Rev. 81 (Part 1) (2018) 912–928, https://doi.org/10.1016/j.rser.2017.08.017.
[18] H. Salem, A.E. Kabeel, E.M.S. El-Said, O.M. Elzeki, Predictive modelling for solar power-driven hybrid desalination system using artificial neural network regression with Adam optimization, ISSN 0011-9164, Desalination 522 (2022) 115411, https://doi.org/10.1016/j.desal.2021.115411.
[19] J. Qin, H. Jiang, N. Lu, L. Yao, C. Zhou, Enhancing solar PV output forecast by integrating ground and satellite observations with deep learning, ISSN 1364-0321, Renew. Sustain. Energy Rev. 167 (2022) 112680, https://doi.org/10.1016/j.rser.2022.112680.
[20] H.M. Abdullah, R.M. Kamel, M. El-Sayed, Non-communication and artificial neural network based photovoltaic monitoring using the existing impedance relay, ISSN 2352-4677, Sustain. Energy, Grids Netw. 22 (2020) 100335, https://doi.org/10.1016/j.segan.2020.100335.
[21] J.F. Roseline, D. Dhanya, S. Selvan, M. Yuvaraj, P. Duraipandy, S.S. Kumar, et al., Neural Network modelling for prediction of energy in hybrid renewable energy systems, Energy Rep. 8 (2022) 999–1008, https://doi.org/10.1016/j.egyr.2022.10.284.
[22] N.P. Weerasinghe, R.J. Yang, C. Wang, Learning from success: a machine learning approach to guiding solar building envelope applications in non-domestic market, J. Clean. Prod. 374 (2022) 133997, https://doi.org/10.1016/j.jclepro.2022.133997.
[23] İ. Kayri, The effects of coolant mass flow rate and atmospheric indicators in a PV/T system with experimental and ANN's models, ISSN 2352-4677, Sustain. Energy, Grids Netw. 36 (2023) 101189, https://doi.org/10.1016/j.segan.2023.101189.
[24] I. Tavares, R. Manfredini, J. Almeida, J. Soares, S. Ramos, Z. Foroozandeh, et al., Comparison of PV power generation forecasting in a residential building using ANN and DNN, IFAC-PapersOnLine 55 (2022) 291–296, https://doi.org/10.1016/j.ifacol.2022.07.051.
[25] C. Ghenai, F.F. Ahmad, O. Rejeb, M. Bettayeb, Artificial neural networks for power output forecasting from bifacial solar PV system with enhanced building roof surface Albedo, J. Build. Eng. 56 (2022) 104799, https://doi.org/10.1016/j.jobe.2022.104799.
[26] D. Kothona, K. Spyropoulos, C. Valelis, C. Koutsis, K.Ch Chatzisavvas, G. C. Christoforidis, Deep learning forecasting tool facilitating the participation of photovoltaic systems into day-ahead and intra-day electricity markets, ISSN 2352-4677, Sustain. Energy, Grids Netw. 36 (2023) 101149, https://doi.org/10.1016/j.segan.2023.101149.
[27] D. Lee, K. Kim, PV power prediction in a peak zone using recurrent neural networks in the absence of future meteorological information, Renew. Energy 173 (2021) 1098–1110, https://doi.org/10.1016/j.renene.2020.12.021.
[28] J. Wang, M. Mae, K. Taniguchi, Uncertainty modeling method of weather elements based on deep learning for robust solar energy generation of building, ISSN 0378-7788, Energy Build. 266 (2022) 112115, https://doi.org/10.1016/j.enbuild.2022.112115.
[29] University of Wisconsin. Solar Energy Laboratory, TRNSYS 17: A transient system simulation program; 2012. http://www.trnsys.com/, accessed on 24 January 2024.
[30] Solar Energy Laboratory, University of Wisconsin-Madison, TRNSYS 17 Documentation, Volume 7, Programmer's Guide, 2012.
[31] R. Perez, R. Stewart, R. Seals, T. Guertin, The Development and Verification of the Perez Diffuse Radiation Model, Sandia Report SAND88-7030, 1988.
[32] Solar Energy Laboratory, University of Wisconsin-Madison, TRNSYS 17 Documentation, Volume 4, Mathematical Reference, 2012.
[33] A.B. Fry, Simulation of Grid-tied Building Integrated Photovoltaic Systems. (M. S. Thesis), Solar Energy Laboratory, University of Wisconsin,, Madison, 1999.
[34] R. Chenni, M. Makhlouf, T. Kerbache, A. Bouzid, A detailed modeling method for photovoltaic cells, Energy, Volume 32, Issue 9, Pages 1724-1730, ISSN 0360-5442. https://doi.org/10.1016/j.energy.2006.12.006.
[35] D.L. King, J.A. Kratochvil, W.E. Boyson, Measuring the solar spectral and angle of-incidence effects on photovoltaic modules and irradiance sensors, Proceedings of the 1994 IEEE photovoltaics specialists conference, Sept 30-Oct 3, 1997, Pages 1113-1116, https://doi.org/10.1109/PVSC.1997.654283.
[36] M.A. Qureshi, F. Torelli, S. Musumeci, A. Reatti, A. Mazza, G. Chicco, A novel adaptive control approach for maximum power-point tracking in photovoltaic systems, Energies 16 (Issue 6) (2023) 2782, https://doi.org/10.3390/en16062782.
[37] J.A. Duffie, W.A. Beckman, Solar Engineering of Thermal Processes, John Wiley & Sons, Inc,, New York, 1991.
[38] P. Kim, Matlab deep learning. With Machine Learning, Neural Networks and Artificial Intelligence, Volume 130, Issue 21, ISBN 978-1-4842-2845-6, 2017, https://doi.org/10.1007/978-1-4842-2845-6.
[39] M.T. Hagan, H.B. Demuth, M.H. Beale, Neural Network Design, PWS Publishing,, Boston, MA, 1996.
[40] M.T. Hagan, M.B. Menhaj, Training feedforward networks with the Marquardt algorithm, ISSN 1941-0093, IEEE Trans. Neural Netw. Volume 5 (Issue 6) (1994) 989–993, https://doi.org/10.1109/72.329697.
[41] Deep Learning Toolbox, ©COPYRIGHT 1992-2004 by The MathWorks, Inc. Natick, Massachusetts, United State, Website: https://www.mathworks.com/help/deeplearning/ref/trainlm.html, Last access: 15/12/2023.
[42] A.H. Elsheikh, S.W. Sharshir, M.A. Elaziz, A.E. Kabeel, W. Guilan, Z. Haiou, Modeling of solar energy systems using artificial neural network: a comprehensive review, ISSN 0038-092X, Sol. Energy 180 (2019) 622–639, https://doi.org/10.1016/j.solener.2019.01.037.
[43] G.D. Garson, Interpreting Neural Network Connection Weights, AI Expert, Volume Issue 6, 1991, Pages 47-51, ISSN 0888-3785.
[44] M. Gevrey, I. Dimopoulos, S. Lek, Review and comparison of methods to study the contribution of variables in artificial neural network models, ISSN 0304-3800, Ecol. Modell. 160 (Issue 3) (2003) 249–264, https://doi.org/10.1016/S0304-3800(02)00257-0.
[45] Canadian Solar Inc, Guelph ON, Canada, Website: https://www.csisolar.com, accessed on 24 January 2024.
[46] Jakson Group, Noida Uttar Pradesh, India, Website: https://www.jakson.com, accessed on 24 January 2024.
[47] LG Electronics, Seoul, Korea, Website: https://www.lg.com, accessed on 24 January 2024.
[48] Panasonic Corporation, Osaka, Japan, Website: https://na.panasonic.com, accessed on 24 January 2024.
[49] Wuxi Suntech Power Co, Wuxi, China, Website: http://suntech-power.com, accessed on 24 January 2024.
[50] Trina Solar Co, Global, Website: https://www.trinasolar.com/en-glb, accessed on 24 January 2024.
[51] M. Kottek, J. Grieser, C. Beck, B. Rudolf, F. Rubel, World map of the Koppen-Geiger climate classification updated, Meteorol. Z. 15 (3) (2006) 259–263, https://doi.org/10.1127/0941-2948/2006/0130.
[52] F. Rubel, M. Kottek, Observed and projected climate shifts 1901-2100 depicted by world maps of the Köppen-Geiger climate classification, Meteorol. Z. 19 (2010) 135–141. ⟨http://koeppen-geiger.vu-wien.ac.at/shifts.htm⟩.
[53] A.J. Arnfield, Köppen climate classification, Encyclopædia Britannica, Encyclopædia Britannica, inc., 2020, https://www.britannica.com/science/Koppen-climate-classification.
[54] S.K. Das, P.K. Basudhar, Prediction of residual friction angle of clays using artificial neural network, Engineering Geology, Volume 100, Issues 3–4, 2008, Pages 142-145, ISSN 0013-7952, https://doi.org/10.1016/j.enggeo.2008.03.001.